

**AUTOMATIC MEASUREMENT OF FEATURES IN ULTRASOUND  
IMAGES OF THE EYE**

**Richard Youmaran**

**Thesis submitted to the  
Faculty of Graduate and Postdoctoral Studies  
In partial fulfillment of the requirements  
For the MASC degree in Electrical Engineering**

**Ottawa-Carleton Institute for Electrical and Computer Engineering  
School of Information Technology and Engineering  
University of Ottawa**

**© Richard Youmaran, Ottawa, Canada, 2005**

*To my family*

## LIST OF ABBREVIATIONS

AOD	Angle Opening Distance
c	Speed of sound
DOF	Depth of field
FWHM	Full Width Half Maximum
Hz	Hertz
ICPD	Iris-ciliary process distance
ID	Iris distance
ILCD	Iris-lens contact distance
IT	Iris thickness
MHz	Megahertz
NL	Non-linear
Np	Nepers
PACG	Primary Angle Closure Glaucoma
R	Reflection coefficient
$\mathfrak{R}^n$	Real number space
TCPD	Trabecular-ciliary process distance
TGC	Time Gain Compensation
UBM	Ultrasound Biomicroscopy
US	Ultrasound
Z	Acoustical impedance
$\psi$	Forward mapping function
$\lambda$	Wavelength
$\sigma^2$	Variance
$\sigma_N^2$	Noise variance

## ABSTRACT

In closed angled Glaucoma, fluid pressure in the eye increases because of inadequate fluid flow between the iris and the cornea. One important technique to assess patients at risk of glaucoma is to analyze ultrasound images of the eye to detect abnormal structural changes. Currently, these images are analyzed manually. This thesis presents an algorithm to automatically identify and measure clinically important features in ultrasound images of the eye. The main challenge is stable detection of features in the presence of ultrasound speckle noise; an algorithm is developed to address this using multiscale analysis and template matching. Tests were performed by comparison of results with eighty images of glaucoma patients and normals against the feature locations identified by a trained technologist. In 5% of cases, the algorithm could not analyze the images; in the remaining cases, features were correctly identified (within 97.5  $\mu\text{m}$ ) in 97% of images. This work shows promise as a technique to improve the efficiency of clinical interpretation of ultrasound images of the eye.

## ACKNOWLEDGMENTS

I would like to take this opportunity and thank my supervisor, Dr Andy Adler, for his support, guidance and understanding. Through the course of my master's studies I have had the great fortune to get to know and interact with him. His comments and suggestions for further development as well as his assistance during writing this thesis are invaluable to me. His talent, diverse background, interest, teaching and research style have provided for me an exceptional opportunity to learn and made be become a better student. In these two years at University Of Ottawa, he has provided me with inestimable support that has significantly impacted my academic life and my future career plans.

I would also like to thank Yednek, Pino and all my fellow students at the VIVA Lab for their constant support and help. We have had many useful discussions that played a major role in my learning process.

Finally, I want to express my deepest appreciation for my fiancée Nadine, my parents Tony and Helen and my brother Roland for being a constant source of loving support and encouragement throughout the years. It is to them that I dedicate this thesis.

## TABLE OF CONTENTS

ABSTRACT.....	iii
ACKNOWLEDGMENTS .....	iv
TABLE OF CONTENTS.....	v
TABLE OF FIGURES.....	viii
Chapter 1.....	2
Introduction.....	2
1.1 Thesis contributions.....	2
1.2 Thesis outline.....	2
Chapter 2.....	4
Ultrasound imaging.....	4
2.1 The Acoustic Spectrum.....	4
2.2 Properties of Acoustic Waves.....	6
2.3 Acoustical Properties of Ocular Tissues in Ultrasound .....	7
2.3.1 Speed of sound.....	8
2.3.2 Attenuation.....	9
2.3.3 Specular reflection .....	9
2.3.4 Scattering .....	12
2.4 Pulse echo Imaging.....	12
2.4.1 A-scan .....	12
2.4.2 B-scan .....	13
2.4.3 Ocular imaging.....	14
2.5 Transducers.....	16
2.6 Relationship between resolution and penetration of the Ultrasound wave.....	17
Chapter 3.....	20
Ultrasound Biomicroscopy .....	20
3.1 History.....	20
3.2 Scanner.....	21
3.3 Image quality .....	21
3.4 Examination techniques in Ultrasound Biomicroscopy.....	22
3.4.1 Patient preparation .....	23
3.4.1.1 Eye cups.....	23
3.5 Producing optimal images.....	25
Chapter 4.....	27
Glaucoma and Ultrasound images of the eye .....	27
4.1 Glaucoma .....	27
4.2 Anatomy of the normal eye.....	28
4.2.1 The cornea.....	31
4.2.2 The sclera .....	31
4.2.3 The iris .....	31
4.2.4 The anterior chamber .....	32
4.2.5 The trabecular-iris angle .....	32
Chapter 5.....	34

Background.....	34
5.1 Wiener Filtering.....	34
5.2 Linear Contrast Stretch.....	35
5.3 Linear edge enhancement.....	36
5.4 Log-Ratio Approach.....	37
5.4.1 Addition $\oplus$ in Image Space.....	38
5.4.2 Multiplication $\otimes$ in Image Space.....	40
5.4.3 Subtraction $\ominus$ in Image Space.....	42
5.4.4 Non-Linear Edge & Contrast Enhancement Algorithm.....	43
5.4.5 Multiscale Representation.....	45
Chapter 6.....	48
Algorithm design.....	48
6.1 STEP 1: Coarse enhancement.....	48
6.1.1 Image thresholding.....	49
6.1.2 Non-Linear Edge & Contrast Enhancement.....	51
6.1.3 Image Binarization.....	51
6.1.4 Image erosion.....	52
6.1.5 Hole Filling.....	52
6.1.6 Template Correlation.....	53
6.1.7 Anterior Chamber Classification and Segmentation.....	54
6.2 STEP 2: Fine enhancement.....	55
6.2.1 Histogram magnification.....	55
6.2.2 Wiener Filtering.....	56
6.2.3 Non-linear Edge & Contrast Enhancement.....	57
6.2.4 Image Binarization.....	57
6.2.5 Image Erosion.....	58
6.2.6 Region expansion.....	58
6.2.7 Region subtraction.....	58
6.2.8 Sclera region classification and segmentation.....	59
6.3 STEP 3: Extra fine enhancement.....	60
6.3.1 Non-Linear Edge & Contrast Enhancement.....	60
6.3.2 Image Binarization.....	61
6.3.3 Sclera region Classification and Segmentation.....	61
6.3.4 Sclera Contour Mapping.....	62
6.3.5 Sclera Contour Smoothing Filter Design.....	63
6.3.6 Scleral Spur Detection.....	64
6.3.7 Determination of Measured Parameters for Glaucoma.....	65
Chapter 7.....	69
Results.....	69
7.1 An example of Outcome 1: Sclera region.....	71
7.2 An example of Outcome 2.....	73
7.3 An example of Outcome 3.....	75
Chapter 8.....	77
Discussion.....	77
8.1 Other areas of application.....	80
8.2 Future work.....	82

8.3 Conclusion .....	86
Bibliography .....	87
Appendix 1: Scleral Spur detection Matlab Code.....	91
Appendix 2: Anterior Chamber region segmentation Matlab Code.....	96

## TABLE OF FIGURES

Figure 1: Ultrasound images of the eye .....	3
Figure 2: The acoustic spectrum .....	5
Figure 3: Interactions of ultrasound with tissue.....	8
Figure 4: Reflection and refraction of an ultrasound pulse with tissue boundary .....	11
Figure 5: A-scan.....	13
Figure 6: (a) Pulse echo imaging .....	15
Figure 7: 50 MHz transducer .....	16
Figure 8: Transducer main components.....	17
Figure 9: Photograph of a focused ultrasound beam .....	18
Figure 10: Lateral resolution versus frequency .....	19
Figure 11: Example of different transducer geometries .....	22
Figure 12: Eyecup installation .....	24
Figure 13: Different size eyecups .....	25
Figure 14: Ultrasound biomicroscopy machine.....	26
Figure 15: A cross-sectional view of the eye.....	29
Figure 16: Raw Image obtained using the UBM machine.....	30
Figure 17: Ultrasound image of the eye showing the iris and other clinical features of interest..	30
Figure 18: Histogram of an image .....	36
Figure 19: Log-Ratio mapping.....	38
Figure 20: Addition in Image Space .....	40
Figure 21: Multiplication in Image Space .....	41
Figure 22: Subtraction in Image Space.....	43
Figure 23: Multiscale Algorithm block diagram showing three stages.....	46
Figure 24: A vertical section of representative images.....	47
Figure 25: Vertical sections of a sample image for parameter selection .....	47
Figure 26: Threshold (THR) selection.....	49
Figure 27: Flowchart illustrating algorithmic steps.....	50
Figure 28: Coarsely enhanced quasi-binary ultrasound image of the eye .....	51
Figure 29: Coarsely enhanced binary image.....	52
Figure 30: Eroded image.....	52
Figure 31: Hole filling .....	53
Figure 32: Template images used for correlation .....	53
Figure 33: Segmented anterior chamber.....	55
Figure 34: Cropped Sclera Region & its corresponding histogram.....	56
Figure 35: Thresholded image .....	56
Figure 36: Wiener filtering .....	57
Figure 37: Finely enhanced image.....	57
Figure 38: Coarsely enhanced image expanded prior to subtraction .....	58
Figure 39: Resulting image after subtraction.....	59
Figure 40: Segmented sclera region.....	60
Figure 41: Extra finely enhanced image .....	61
Figure 42: Extra finely enhanced sclera region segmented .....	61

Figure 43: Contour mapping .....	62
Figure 44: Smoothed sclera contour .....	63
Figure 45: Lower contour of the iris re-adjusted .....	66
Figure 46: AOD 500 Calculation Diagram .....	67
Figure 47: Original image showing the computed clinical parameters of interest .....	68
Figure 48: Offset pixel error histogram .....	71
Figure 49: Example of an outcome 1 .....	72
Figure 50: Example of an outcome 2 .....	75
Figure 51: Example of an outcome 3 .....	76
Figure 52: Ultrasound prostate image enhancement using the <i>sticks</i> method .....	81
Figure 53: Enhanced prostate ultrasound image using our developed algorithm .....	81
Figure 54: Ultrasound images of the prostate .....	82
Figure 55: Clinical UBM parameters .....	84
Figure 56: Iris thickness before and after treatment with 2% ibopamine .....	85

# Chapter 1

## Introduction

Glaucoma is one of the leading causes of blindness. In closed angled Glaucoma, fluid pressure in the eye increases because of inadequate fluid flow between the iris and the cornea. To illustrate the structural changes due to this condition, cross sectional ultrasound images are shown in Figure 1. Figure 1 (a) and (b) show ultrasound images of a healthy and a diseased eye, respectively. Figure 1 (b) shows an eye with a closed-angle as a result of the fluid pressure in the eye that causes damage and eventually death of nerve fibers responsible for vision (Deepak, 2002). One important technique to assess patients at risk of glaucoma is to analyze ultrasound images of the eye to detect the structural changes that reduce the flow of fluids out of the eye (Pavlin *et al*, 1991). Usually, sequences of ultrasound images of the eye are analyzed manually; a trained technologist determines anatomical feature locations and measures the relevant clinical parameters (Pavlin, 1995). We are unaware of any work to develop an automated algorithm to analyze these images. The main features within the eye of clinical interest are: the sclera, a dense, fibrous opaque white outer coat enclosing the eyeball except the part covered by the cornea; the scleral spur, a small triangular region in a meridional section of the sclera tissue with its base along the inner surface of the sclera; the anterior chamber, the region bounded by the posterior surface of the cornea and the central part of the lens; and, the trabecular-iris recess, the apex point between the sclera region and the iris (Figure 15). Manual analysis of eye images is fairly time consuming, and the accuracy of parameter measurements varies between experts (Nishijima *et al*, 2000). To address these issues, the goal of this thesis is to develop an algorithm to automatically analyze eye ultrasound images and locate all the features of interest within the

image. The difficulties in measuring these parameters are associated with noise, poor contrast, poor resolution, and weak edge (boundary) delineation inherently present in ultrasound images (Pathak *et al*, 2000). We anticipate that this scheme will reduce the processing time currently taken by the technologist to analyze patient images and extract the clinical parameters of interest.

## **1.1 Thesis contributions**

This thesis describes a new method to detect features in ultrasound images, which shows good performance in detection of difficult features. The developed technique makes use of major image processing methods and fundamentals. In order to calculate the clinical parameters of interest, new region classification and segmentation techniques are developed as well as some signal processing to locate the scleral spur. The ultrasound images of the eye are very noisy, with poor resolution and weak edge delineation, which required the development of a three step method to overcome these challenges. The complete algorithm is shown in Figure 23.

## **1.2 Thesis outline**

The thesis is organized as follows: Chapter 2 and Chapter 3 present an introduction to Ultrasound imaging and Ultrasound biomicroscopy (UBM) respectively. Chapter 4 describes the Glaucoma disease and presents the major features of interest in the ultrasound image of the eye that are used by the algorithm to compute the trabecular-iris angle. Overviews of the image processing techniques used for feature identification are introduced in Chapter 5. Chapter 6 describes the automated algorithm for feature detection and extraction, including speckle reduction methods, non-linear contrast and edge enhancement, template correlation, region

segmentation and classification, and computation of clinical parameters. Chapter 7 presents experimental results obtained from testing the algorithm. Finally, Chapter 8 presents a discussion of previous work done in this field and concludes this work.

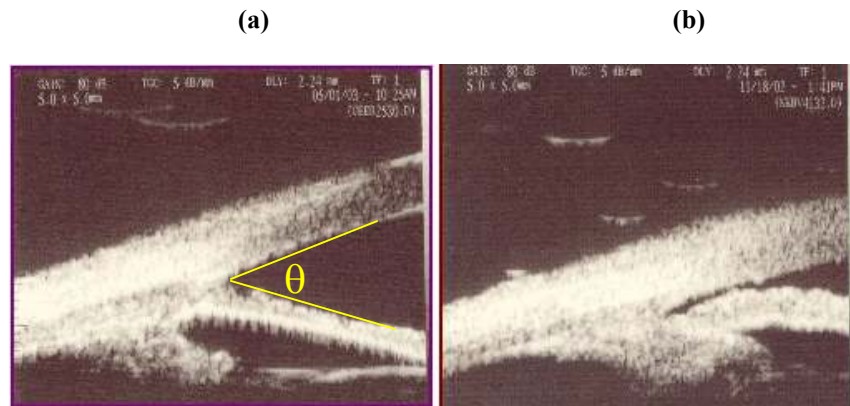


Figure 1: Ultrasound images showing (a) normal eye (open angle  $\theta > 0$ ) (b) diseased eye (closed-angle  $\theta \approx 0$ )

# Chapter 2

## Ultrasound imaging

Medical ultrasound is an imaging modality widely used for many clinical applications. Ultrasound images are obtained by transmitting high frequency sound waves into the part of the body to be imaged and then capturing and processing the reflected signals from the different tissues of the region of interest (Pavlin *et al*, 1995). Ultrasound imaging provides a cross-section of the soft-tissue volume under investigation; however, it cannot be used to image bone and bodies of gas such as found in lungs. It is widely used clinically; it has the advantage of being a real-time modality that does not use any ionizing radiation and can provide quantitative measurement and imaging of blood flow. This chapter explains the basic physics of high-frequency ultrasound imaging.

### 2.1 The Acoustic Spectrum

The acoustic spectrum is the range of frequencies where mechanical waves and vibrations occur. It extends from the audible range (10-20000 Hz) to the range of phonons ( $10^{12}$  Hz). Generally, medical applications in ultrasound extend from 1 to 10 MHz on the spectrum (Figure 2). As the frequency increases, wave penetration is reduced since it undergoes stronger attenuation in the body. However, an increase in the wave frequency results in greater image resolution. For example, frequencies between 3 and 5 MHz are used to image large body parts at a depth of 15 to 20 cm. Frequencies between 7

and 10 MHz can be used to image smaller parts of the body such as the eye where only 4-5 cm of penetration is needed. Lately, new medical applications make use of high-frequency ultrasound between 10 and 50MHz to image the skin (Pavlin *et al*, 1995, Forster *et al*, 1996, Yano *et al*, 1987), the gastrointestinal tract (Wiersema *et al*, 1989, Silverstein *et al*, 1989), and blood vessels (via intravascular imaging) (Pandian, 1989, Yock *et al*, 1989, Hosgson *et al*, 1989). The ultrasound biomicroscopy frequency range extends from 40 to 100 MHz and is mainly used to image body parts at a reduced depth since, at these frequencies, ultrasound waves are highly attenuated. Hence, the eye presents an ideal clinical application for UBM because of its anatomical position at the body surface permits high-resolution images to be resolved at a reduced depth. Section 2.2 describes the interactions of acoustic waves with ocular tissue including attenuation, speed of sound and reflectivity.

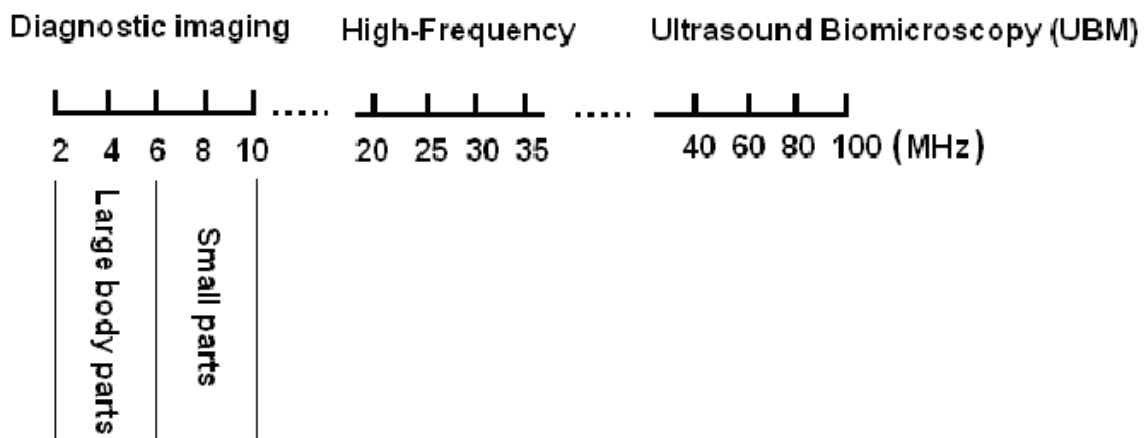


Figure 2: The acoustic spectrum showing the UBM imaging frequency range (taken from Pavlin and Foster (1995))

## 2.2 Properties of Acoustic Waves

In order to derive an expression for the time and spatial dependence of a pressure wave (Heath, 1999, Pavlin *et al*, 1995), we first take a snapshot (i.e. independent of time) of a propagating sound wave at a specific time and represent it mathematically as follows:

$$\begin{aligned} p(z) &= \sin\left(\frac{2\pi}{\lambda} z\right) \\ &= \sin(kz) \end{aligned} \quad (1)$$

where  $k = \frac{2\pi}{\lambda}$  is the wave number (rad/m),  $\lambda$  is the wavelength (m) and  $z$  is the direction of propagation. To examine the time-dependence of the pressure wave in space, it is necessary to fix our position in space and measure pressure variations at that point with time, which results in a sinusoidal expression described by the equation:

$$\begin{aligned} p(t) &= \sin\left(\frac{2\pi}{T} t\right) \\ &= \sin(2\pi ft) \end{aligned} \quad (2)$$

where  $T$  is the period of the wave,  $f$  the frequency and  $t$  the time. A complete time-spatial representation of the pressure wave is derived by combining equations 1 and 2 to obtain the following:

$$p(z, t) = \sin(2\pi ft - kz) \quad (3)$$

where the amplitude of the pressure wave  $p(z,t)$  is dependent on both position and time coordinates. The relationship  $\lambda=cf$  between speed of sound ( $c$ ), frequency ( $f$ ) and wavelength ( $\lambda$ ) is also worth mentioning. This relationship illustrates that the wavelength of ultrasound is an important factor in determining image resolution.

### **2.3 Acoustical Properties of Ocular Tissues in Ultrasound**

Attenuation, reflectivity and speed of sound are tissue characteristics that are important in ultrasound imaging. The attenuation process, which involves energy removal from the beam, is divided into two categories (Pavlin, 1995): absorption and reflectivity (Figure 3). The absorption process contributes very little in the image formation process since it only implies a transformation of the absorbed energy into heat. The following are the main processes that cause the transformation of acoustic energy into thermal energy: (a) frictional losses, (b) heat conduction losses, and (c) molecular exchange of energy. On the other hand, differences in tissue reflectivity provide most of the information required to construct an ultrasound image. The reflectivity depends on both the shape and the nature of the tissue being imaged (Nicholas, 1977). In this text, reflectivity is subdivided into two components: scatter and specular reflection. Scattering refers to the interaction of the ultrasound wave with particles that are smaller than the sound's wavelength, while specular reflections arise at larger tissue interfaces (Anderson *et al*, 2000). The scattering or reflection of the acoustic waves arises from inhomogeneities in the medium's density and compressibility. Among all these processes, the main contribution in image formation is due to near normal incidence specular reflection.

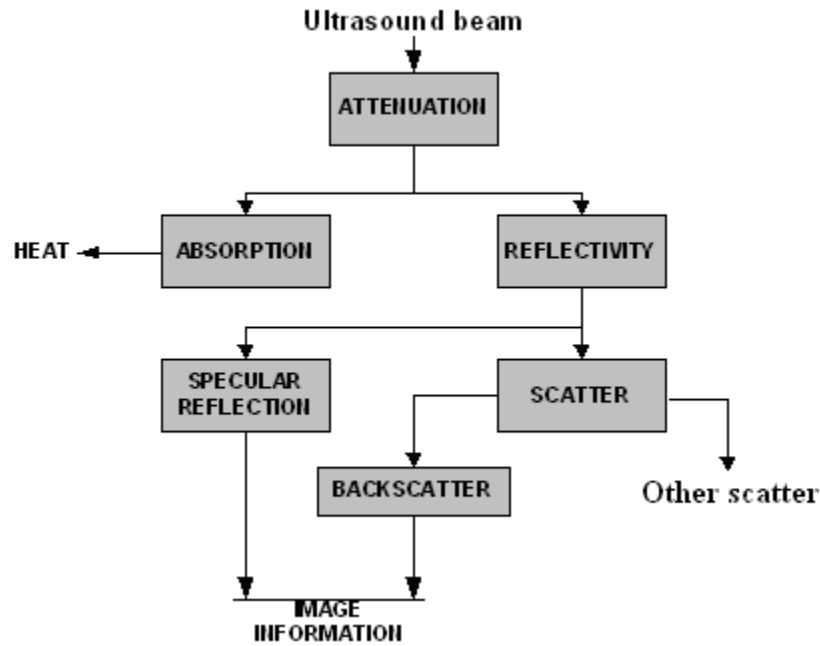


**Figure 3: Interactions of ultrasound with tissue. Only specular reflection and backscatter contribute in image formation (taken from Pavlin and Foster (1995))**

### 2.3.1 Speed of sound

The speed of sound is roughly constant in different soft tissues. Because of this, it can be used to approximate distance measurements in ultrasound images. Many researchers have measured the speed of sound in ocular tissues to be in the range of 1550 to 1650 m/s (Begui, 1954, Jansson *et al*, 1961, Rivara *et al*, 1962, Thijssen *et al*, 1983). The speed of sound allows the conversion of propagation time of ultrasound waves in the tissue into distance in the image (section 2.4). The speed of sound for soft tissues is approximated to 1540 m/s, 1622 m/s for scleral tissue, 1580 m/s for the cornea, 1554 m/s in ciliary muscle and 1542 m/s in the iris (Thijssen *et al*, 1983, Ye *et al*, 1995, Goss *et al*, 1978).

### 2.3.2 Attenuation

The attenuation mechanism in ultrasound imaging is directly related to the tissue being imaged and to the propagating wave frequency. This mechanism is attributed to a relaxation process in which energy is removed from the beam by an oscillating particle and then returned at a later time (Woodcock, 1979). The wave amplitude in soft tissues is proportional to the attenuation coefficient ( $\alpha$ ) under the assumption that homogeneous tissues exhibit a simple exponential loss of pressure amplitude as the wave propagates. Therefore, the pressure distribution in an ultrasound field can be written as follows:

$$p(z) = p_0 e^{-\alpha z} \quad (4)$$

where  $p_0$  is the initial pressure amplitude and  $\alpha$  (Np/mm) is the attenuation coefficient in the tissue including both absorption and scattering. For the eye, the scleral tissue (section 4.2) has the highest attenuation followed by the ciliary body, the iris and the cornea (Ye *et al*, 1995). At 50 MHz, the attenuation in the ocular tissue ranges from 1.3 dB/mm for the cornea to 4.3 dB/mm for the sclera.

### 2.3.3 Specular reflection

When tissue structures within the body form boundaries on a scale much larger than the wavelength, specular reflection arises. An incident ultrasonic wave impinging on an interface between two media at an angle  $\theta_i$  is reflected back at an angle  $\theta_r = \theta_i$ . As in optics, Snell's law (Bovik, 2000) can be used in ultrasound to calculate the refraction of ultrasonic waves when traveling between two media of differing acoustic properties

(Figure 4). When an incident wave hits a boundary between two different media, reflected and transmitted waves are generated with different amplitude and orientation depending on the initial direction of the beam and the characteristics of the medium. This relationship can be written as:

$$c_2 \sin \theta_t = c_1 \sin \theta_i \quad (5)$$

where  $c_i$  is the speed of sound in the corresponding tissues. In order to define the pressure reflection coefficient  $R$ , we must introduce the acoustical impedance parameter  $Z$ , which describes the elastic properties of the tissue as:

$$Z = \rho c \quad (6)$$

where  $\rho$  is the density of the tissue and  $c = 3 \times 10^8$  m/s. Assuming normal incidence, the reflection coefficient becomes:

$$R = \frac{Z_2 - Z_1}{Z_2 + Z_1} \quad (7)$$

where  $Z_i$  describes the elastic properties of medium  $i$ . In Thijssen *et al* (1983), acoustical impedances of several eye tissues and their reflection coefficient were measured as seen in table 1.

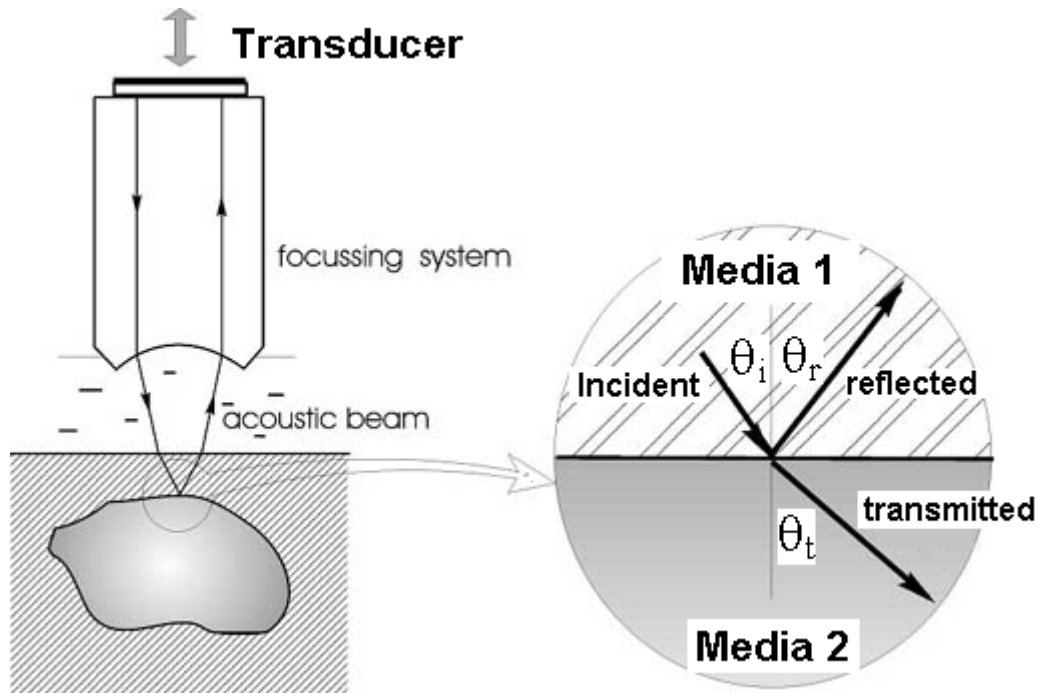


Figure 4: Reflection and refraction of an ultrasound pulse with tissue boundary (taken from [www.tech-dm.com/micro.htm](http://www.tech-dm.com/micro.htm))

Tissue	Z	R (dB) in water
Cornea	1.55	- 41.8
Sclera	1.61	- 31.3
Retina	1.55	- 41.8
Lens	1.73	- 24

Table 1: Acoustical impedances ( $Z_i$ ) and reflection coefficient (R) of several eye tissues

In a case where a severe acoustical impedance mismatch occurs (i.e. boundary between tissue and air), almost all sound wave energy is reflected and no energy is further transmitted in the tissue. This explains why ultrasound cannot image tissues within or lying under the lung.

### **2.3.4 Scattering**

Scattering processes cause ultrasonic energy to be spread off the axis of the ultrasound beam, due to a deflection of sound waves by particles or medium inhomogeneities. Backscattered rays (ultrasound waves reflected back to the direction they came from) are the only ones in the scatter category that contribute to image information. Scattering arises from targets with a size comparable or smaller than the wavelength. If the placement of these scatterers is spatially random, the resulting incoherent scattering gives rise to speckle noise. If the scatterers have a periodic arrangement, a coherent component is introduced, producing periodicity in the image (Anderson *et al*, 2000). Backscattered ultrasound energy returns to the transducer where it is used in the image formation process. At the ultrasound transducer, constructive and destructive interference take place to create regions with speckled texture, which varies for each tissue being imaged. Due to this reason, ultrasound images are noisy and contain poor boundary delineation between different tissues.

## **2.4 Pulse echo Imaging**

Ultrasound imaging can be used in many modalities. The A-scan and B-scan are two different formats for displaying ultrasound echo data, relevant to this thesis.

### **2.4.1 A-scan**

An A-scan (or A-mode) is a one-dimensional ultrasonic display showing echoes along the ultrasonic beam as vertical spikes on a horizontal time axis indicating the depth of the reflectors (Figure 5). The amplitudes of the spikes are directly proportional to the echo strengths after time gain compensation (TGC), and the horizontal position (left-right) of

the spikes is determined by the time difference between the transmission of the ultrasound pulse and the arrival of the echo at the transducer (Anderson, 2000). An A-scan signal calculates the distance (or depth) into the tissues from the time taken by an ultrasound pulse using the following equation:

$$z = \frac{ct}{2} \quad (8)$$

where  $z$  is the distance measure,  $t$  is the time taken by the pulse to travel back to the transducer, and the factor 2 takes into account the fact that a pulse travels the same distance twice when it reflects on a boundary.

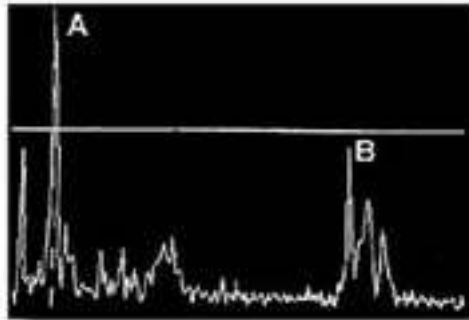


**Figure 5:** An example of an A-scan showing two peaks (A and B) corresponding to two objects with different consistency and hardness (taken from [www.frca.co.uk/ Images](http://www.frca.co.uk/Images)). The horizontal axis corresponds to depth while the y-axis reflects wave amplitude.

#### 2.4.2 B-scan

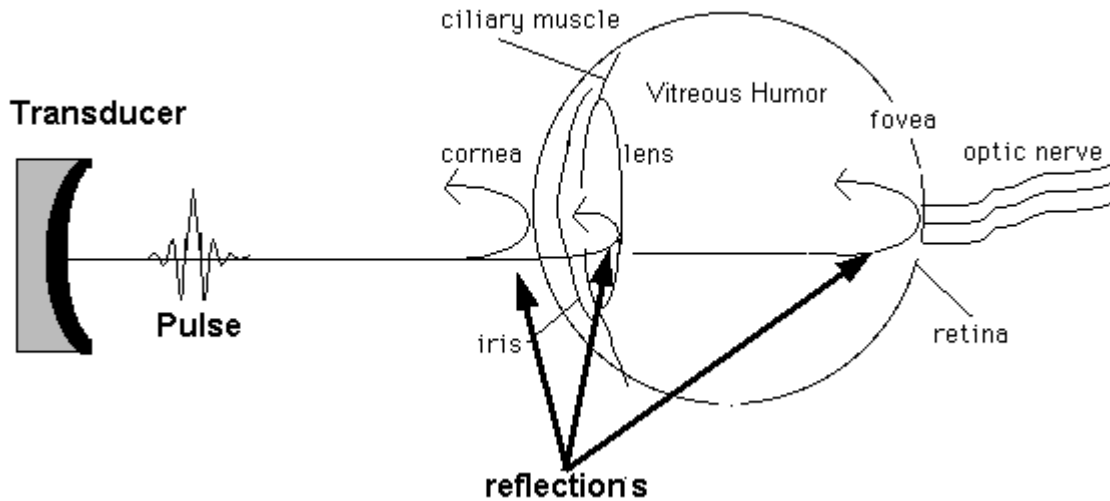
A two-dimensional image or B-scan images the reflectivity of a two-dimensional slice through a portion of the anatomy. It is composed of pixels representing the ultrasound

echo amplitude after TGC. The B-scan is formed by coding the A-scan line as brightness along one line of sight and then by linearly scanning the transducer at a uniform velocity. The B-scan needs some kind of mechanical or electronic technique to radially sweep the US beam into the tissue. One way of achieving a sector sweep is using the phased array method where a phase difference is introduced between adjacent transducing sources to flex the plane wave front, without having to mechanically move the transducer. Since a B-scan is made of many different beams, it has a much lower imaging rate than the A-Scan.

### **2.4.3 Ocular imaging**

The first applications of ultrasound in ocular imaging were first demonstrated by Mundt *et al.* (1956). Ossoing (1979) developed standardized methods to interpret one-dimensional ultrasound images of the eye, also known as “A-mode”. Baum (1956), Coleman (1977) and many others made significant contributions in the two-dimensional or “B-mode” ultrasound imaging technology. Figure 6 illustrates an ocular imaging system where a transducer generates a pulse in response to an electrical simulation, which propagates in the coupling medium at the speed of sound. At each boundary between different tissues in the eye, a fraction of the pulse is reflected back to the transducer and the other transmitted through the medium (Figure 6(a)). The first reflection is seen at the boundary between the coupling medium and the cornea, the second between the lens and the vitreous humor, and the third at the fovea. The received echoes are then converted to radio frequency electrical signals by the transducer (Figure 6(b)), amplified and demodulated (A-scan).

(a)



(b)

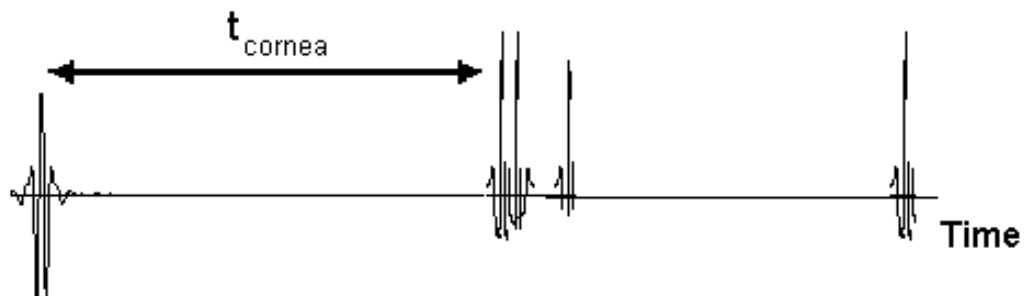


Figure 6: (a) Pulse echo imaging where the transducer generates an ultrasound pulse in response to an electrical simulation. The pulse propagates through a coupling medium and then is partially reflected at each impedance discontinuity within the eye, (b) Reflected ultrasound pulses are converted into radio frequency signal using time of propagation (taken from Pavlin and Foster (1995))

## 2.5 Transducers

The transducer in ultrasound imaging is responsible for converting electrical energy into acoustical energy and vice versa, and its design determines the image resolution, contrast and sensitivity. A transducer (Figure 7) is mainly composed of an active piezoelectric material, a matching layer and a backing (Figure 8). The piezoelectric material is chosen with a thickness that causes it to vibrate at the resonant frequency of the scanner. Depending on the imaging application, the backing and matching layers acoustical properties are carefully selected in order to generate adequate high-frequency ultrasound pulses.



**Figure 7: 50 MHz transducer (taken from Deepak (2002))**

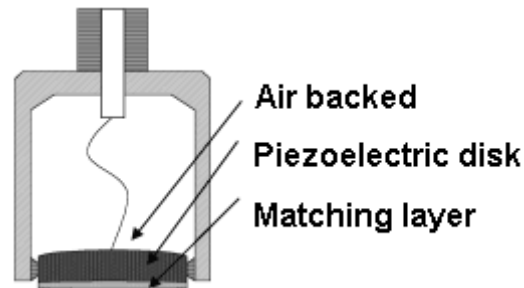


**Figure 8: Transducer main components showing the low impedance matching layer, the piezoelectric material and a backing**

## **2.6 Relationship between resolution and penetration of the Ultrasound wave**

In ultrasound, a major tradeoff exists between resolution and beam penetration in the tissue. As the frequency of the ultrasound pulse increases, better resolution is achieved; however, the ultrasound wave undergoes higher attenuation, limiting its ability to penetrate deeper in the tissue (Figure 10). Another factor that limits the depth at which an ultrasound beam can image a tissue is beam divergence. An ultrasound beam tends to diverge with distance no matter at which frequency it is operating. For this reason, optimal imaging is achieved when the tissue is within the depth of field (DOF) of the transducer (Figure 9) estimated to:

$$L_{DOF} = \frac{d}{\lambda} \quad (9)$$

where  $L_{DOF}$  is the depth of field,  $d$  is the diameter of the transducer, and  $\lambda$  is the wavelength. Generally, the beam remains well focused within the depth of field region (DOF) (Figure 9). The larger the transducer, or the smaller the wavelength, the greater the DOF.

The lateral resolution is related to the full width of the ultrasound beam at half maximum amplitude (FWHM) as:

$$FWHM = \frac{cR}{fd} \quad (10)$$

where  $f$  is the frequency,  $R$  and  $d$  are the focal length and the diameter of the transducer, respectively. The best focus is achieved at the focal length of the transducer. In the axial direction, it is found that the resolution is proportional to the length of the ultrasound pulse and thus to the pulse frequency and bandwidth. The smallest resolvable distance ( $\Delta z$ ) between two planar surfaces becomes:

$$\Delta z = \frac{cW_{temp}}{2} \quad (11)$$

where  $W_{temp}$  is the temporal width of the pulse at one-half maximum.

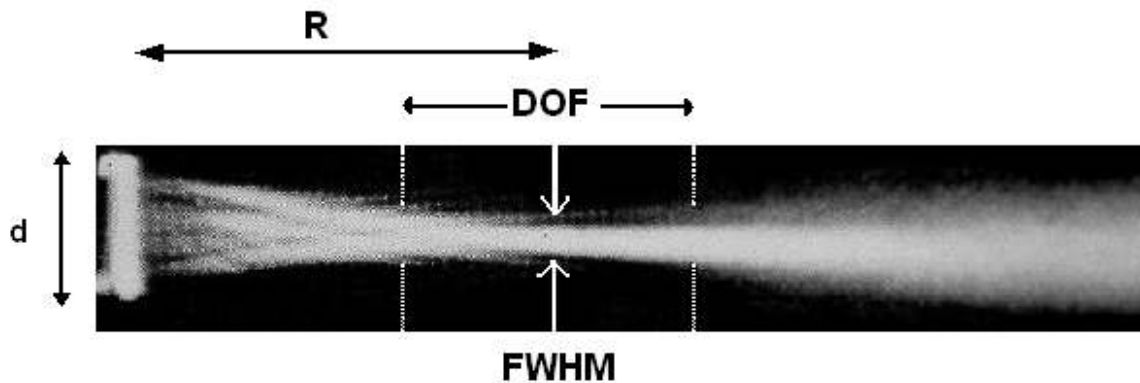


**Figure 9: Photograph of a focused ultrasound beam taken in 1975 in the ultrasound laboratory at the Bowman Gray School of Medicine. The lateral resolution is proportional to FWHM of the ultrasound beam (taken from *OBGYN.net*)**

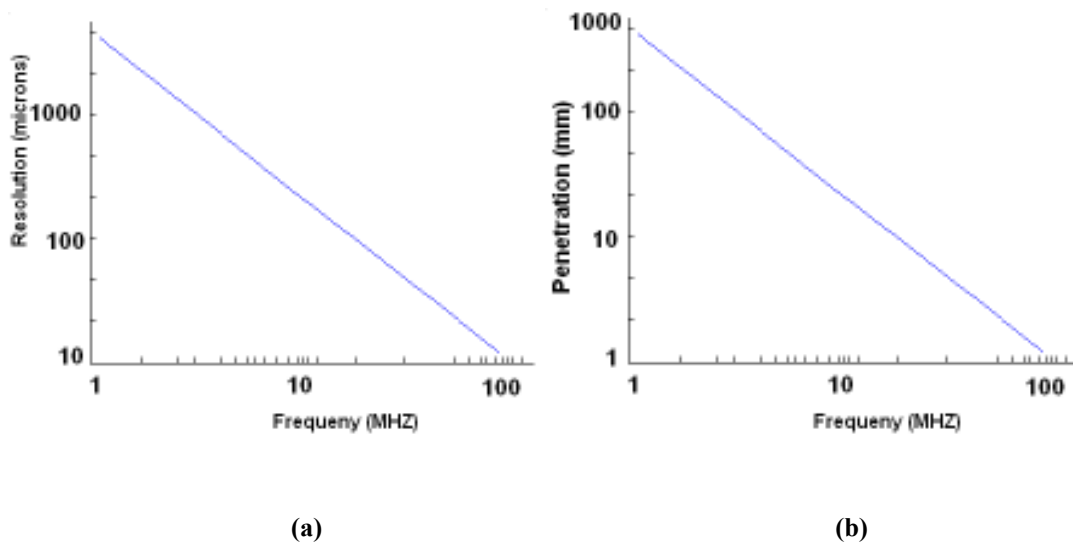


Figure 10: (a) Plot of lateral resolution versus frequency, (b) Plot of penetration versus frequency under realistic imaging conditions. As frequency increases, resolution is better except that penetration of the beam is reduced due to increase in losses in the tissues

# Chapter 3

## Ultrasound Biomicroscopy

Ultrasound biomicroscopy is a recent imaging modality used to image the eye using high-frequency transducers. It differs from traditional ultrasound imaging by the use of high-frequency transducers that image body structures at smaller depth with a higher resolution (Pavlin, 1995, Yano *et al*, 1987). The transducer used for B-scan (posterior segment evaluation) operates at a frequency close to 10 MHz where the probe targets structures at a depth of 4 cm with a resolution of 940 microns. This is well suited for the posterior segment since all the structures at this depth have a thickness greater than 1 mm. On the other hand, the anterior segment has a depth of 4-6 mm allowing the use of higher frequency probes. UBM plays a major role in imaging these structures, which are usually spaced very close to each other, by operating 50 MHz probes with a resolution of 40 microns at a depth of 4mm.

### 3.1 History

In 1989, Charles and Foster at the Princess Margaret Hospital in Toronto, Canada developed the UBM machine. At this time, they built three probes operating at 50, 80 and 100 MHz to image different structures in the eye (Sherer *et al*, 1989). After multiple experiments, they demonstrated that a 50 MHz transducer is ideal to image the eye since it provides a good compromise between depth and resolution. In 1991, Zeiss developed the first commercial UBM machine with only one probe available, operating at 50 MHz.

The main components and characteristics of the UBM machine are discussed in more detail in the next section.

### **3.2 Scanner**

The operating frequency in a UBM system is approximately an order of magnitude higher than conventional B-mode imaging. The achievement of real-time B-mode imaging at such frequencies required the development of new technology in the following areas: (1) transducers, (2) high-frequency signal analysis and (3) precise motion control. In order to collect radio-frequency ultrasound data, a 40 to 100 MHz transducer is moved linearly over the imaging field (4mm) collecting information at each 512 equally spaced lines with a distance of 8  $\mu\text{m}$  between the lines (Deepak, 2002, Pavlin, 1995). A high voltage (200 V peak-to-peak) of 40 to 100 MHz pulse is applied to excite the transducer, which results into a 40-100 MHz ultrasound pulse transmitted in the tissue. The backscattered ultrasound is received by the same transducer and amplified using time-gain compensation techniques. Afterwards, the signal is non-linearly processed and demodulated to produce the A-scan, which is converted to digital format and displayed as brightness on a video monitor. B-mode imaging is performed at 5 to 10 frames/sec.

### **3.3 Image quality**

The frequency of the ultrasound, the ratio of the focal length to the transducer diameter and the length of the pulse affect the image quality enormously (Heath, 1999, Jansson *et al*, 1961). Figure 11 shows transducers with different diameter, focal lengths and frequency. Transducers with smaller frequency tend to have a larger depth of field and

can penetrate a tissue and image deeper structures. However, at 50 MHz, not all eye structures can be resolved adequately. For example, to resolve the corneal epithelium (section 4.2), an 80 MHz device is needed to provide a clear image. For this reason, the frequency at which a transducer is operating must be carefully selected based on the application.

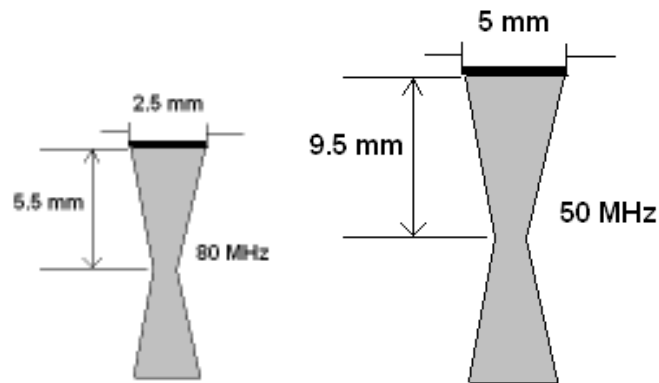


**Figure 11: Example of different transducer geometries that varies with ultrasound frequency and that are used in different application (taken from Pavlin 1995)**

### 3.4 Examination techniques in Ultrasound Biomicroscopy

An ultrasound biomicroscopic examination has a lot in common with a conventional B-scan ultrasound. The transducer is placed opposite to the imaged area and the probe is carefully manipulated with reference to the screen image to produce optimal results. The main differences between UBM and conventional B-scan are: the use of a moving transducer without a covering membrane since the latter attenuates the wave, and moves the transducer further from the region to be evaluated. Because of the lack of cover membrane, UBM needs to image in a water bath as a coupling medium.

### 3.4.1 Patient preparation

For the examination procedure, an eyecup, a saline solution and a fluid-coupling medium are needed (Pavlin *et al*, 1995). The patient is placed in a supine position during examination. Some form of fixation device is used at which the patient is asked to look with the non-examined eye during the procedure. This will ensure that the patient's eye remains stable during the imaging process. Normally, the monitor is placed at an adequate height where the operator can easily observe. Also, the hand controller should be easily accessible without the need to move the patient.

#### 3.4.1.1 Eye cups

A series of eyecups are used during examination in order to facilitate the procedure. They are similar to eyecups used for A-scan biometry (Ossoinig, 1979) with the bottom of the module that fits between the lids of the eye to hold them open. Since in UBM the working distance is relatively small, eyecups do not have to be as high as conventional biometry cups. Also, they are designed to have a flared opening in order to improve transducer mobility during examination. These cups come in different diameters where 22 to 24 mm is suitable to examine adult eyes (Deepak, 2002). Before placing the eyecup in the patient's eye, a topical anesthetic is instilled and the superior lip of the cup is then placed under the upper lid. Afterwards, the lower lid is drawn down by the operator and placed over the inferior lip. Once the eyecup installation is completed, it is then filled with fluid to produce a coupling medium between the transducer and the eye, since ultrasound propagates in air very poorly. The fluid used is chosen to have a low attenuation and to be absolutely safe for the eye. It also needs to be viscous in order to

prevent fluid loss when the operator moves around the cup. 1 to 2.5% Methylcellulose has shown to be a good fluid for these applications since it has minimal sound attenuation and not very irritating for the eye (Pavlin *et al*, 1995). Once the eyecup is well placed and filled with the coupling fluid, it is necessary to remove all air bubbles in the fluid and on the tip of the transducer since these can significantly attenuate sound waves. Large air bubbles can be removed with a cotton swab.



**Figure 12: Eyecup placed in between the eyelids (taken from Deepak (2002))**

During examination, extra care should be deployed by the operator when manipulating the transducer because the tip is not covered by a protective membrane. The latter device is moving at a rate of 8 passes per second, thus any contact with the cornea could produce corneal abrasion. One solution to this problem is the use of soft contact lens on the cornea. A high water content disposable soft contact lens is preferred since it causes less attenuation compared to the regular one. Contact lenses become crucial when the operator is imaging deep structures in the eye since the transducer has to be placed very close to the cornea.



**Figure 13: Different size eyecups (taken from Deepak (2002))**

### **3.5 Producing optimal images**

The Zeiss-Humphrey Inc. instrument is used for UBM measurements in this thesis. This machine (Figure 14) runs at approximately 50 MHz, which offers a reasonable compromise between resolution and penetration, and works well for eye examination (Pavlin, 1995). In order to obtain ideal images, the ultrasound beam should be directed perpendicular to the structures being examined in order to receive the greatest return of reflected sound to the transducer. The operator can use the image on the screen as an indicator of perpendicularity since images are brightest when the probe is perpendicular to the surface being examined. Depending on the information that the operator is seeking, the probe can be rotated and moved vertically or horizontally.

In UBM images, the front of the transducer corresponds to the top of the screen; a structure observed at the top of the screen is closest to the probe. In practice, the operator is constantly making fine adjustments to aim an accurate beam towards a target region and produce sections that show pathological changes clearly. This requires an experienced technician with a lot of coordination and precision.



**Figure 14: Ultrasound biomicroscopy machine (taken from Deepak (2002))**

# Chapter 4

## Glaucoma and Ultrasound images of the eye

UBM is an important tool for the study of Glaucoma. It allows measuring the degree of angle closure in eyes with Primary Angle Closure Glaucoma (PACG) (Pavlin *et al*, 1995). With the UBM, the trabecular-iris angle can be directly visualized and calculated using features and landmarks in the ultrasound image of the eye. This section describes the major features of the eye imaged using UBM, which are necessary for the angle calculation.

### 4.1 Glaucoma

Glaucoma is the term for a diverse group of eye diseases, all of which involve progressive damage to the optic nerve of the eye. In closed angled Glaucoma, fluid pressure in the eye increases because of inadequate fluid flow between the iris and the cornea. The pressure causes damage and eventually death of nerve fibers responsible for vision (Deepak, 2002). One important technique to assess patients at risk of glaucoma is to analyze ultrasound images of the eye to detect the structural changes that reduce the flow of fluids out of the eye (Pavlin *et al*, 1991). The ability of UBM to image the anterior chamber structures at high resolution makes it a very important tool to study Glaucoma.

## **4.2 Anatomy of the normal eye**

This section will discuss UBM appearance of anatomical features and structures of the normal eye. UBM provides a view of subsurface structures and allows defining measurement sites in terms of fixed anatomical landmarks (Figure 16). Some difficulties arise since the position of some structures varies with internal dynamic changes such as those arising with light exposure. In order to overcome this problem, repeated examinations should be completed under similar conditions, as well as having measurements taken in the same orientation. Figure 17 illustrates features of interest in the ultrasound image of eye used for defining measurement sites and calculating the position of important landmarks.

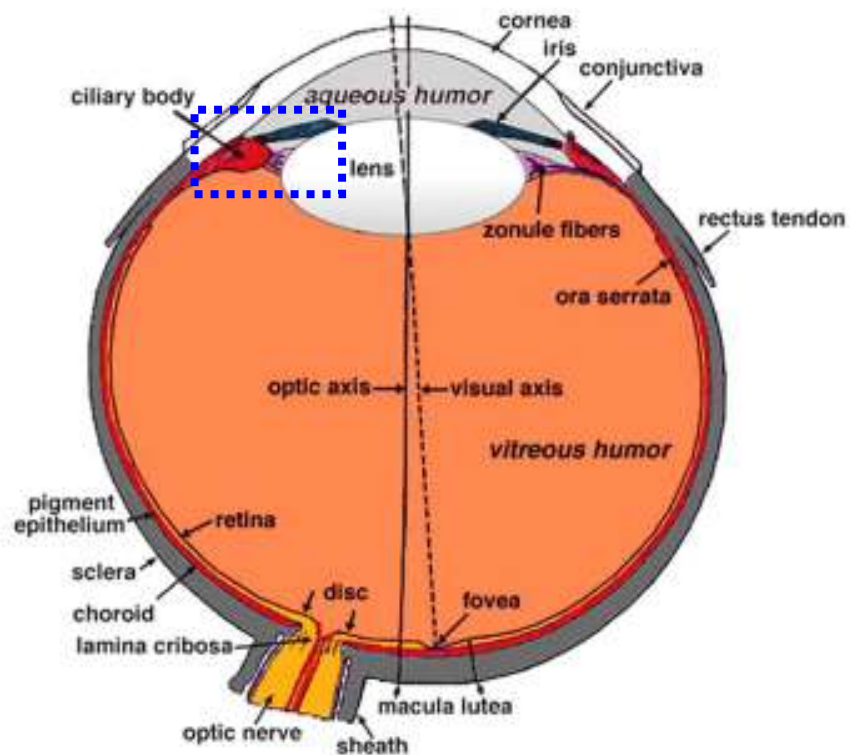
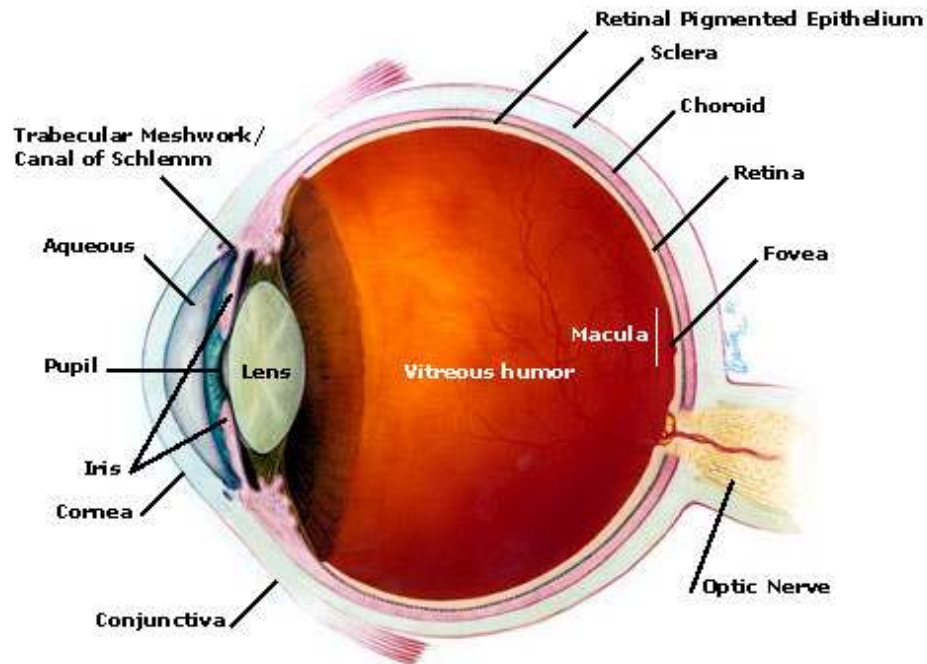


Figure 15: A cross-sectional view of the eye showing major parts. The outlined region shows the section of the eye that is imaged by UBM. Images are taken from <http://webvision.med.utah.edu/anatomy.html>



Figure 16: Raw Image obtained using the UBM machine

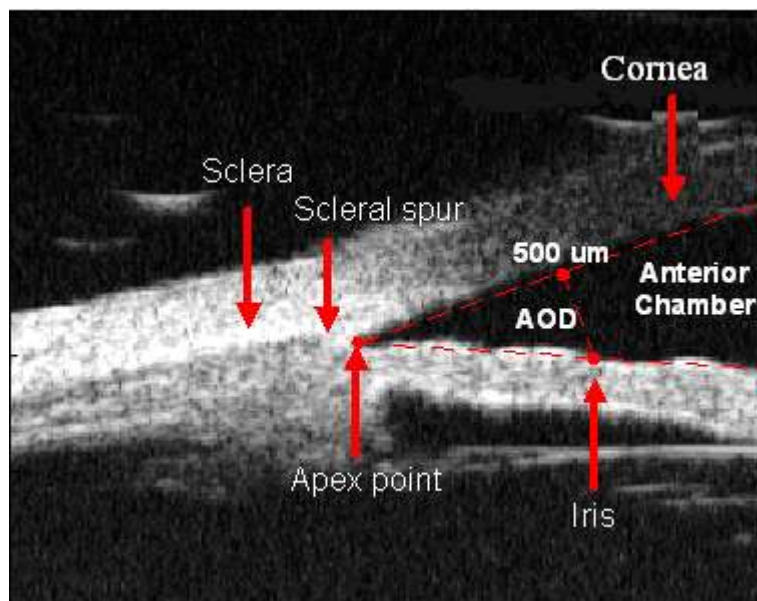


Figure 17: Ultrasound image of the eye showing the iris and other clinical features of interest located within the outlined region in Figure 15.

### **4.2.1 The cornea**

The cornea is the outer, transparent, dome-like structure that covers the iris, pupil, the anterior chamber and that is continuous with the sclera (Figure 15). Imaging the cornea is accomplished with high-frequency high-resolution transducers since the depth of penetration in the tissue is not of a great importance due to the superficial location of this eye structure. Corneal studies have been done with 75 to 100 MHz transducers. Studies in vitro (Ye *et al*, 1995) have shown that the cornea has a lower internal reflectivity than the sclera, which allows differentiating between these regions in the ultrasound image of the eye. In fact, the scleral backscatter coefficients exceed those of the cornea by a factor of 4.6 (Pavlin *et al*, 1995). As seen in Figure 17, the sclera region is brighter compared to other regions in the ultrasound image of the eye since it has higher internal reflectivity.

### **4.2.2 The sclera**

The sclera is the tough white fibrous outer envelope of tissue covering the entire eyeball except the cornea (Figure 15). The high reflectivity of the sclera allows it to be well differentiated from other, less reflective, ocular tissue. The sclera is an important feature in the eye since it encloses the scleral spur, a major landmark for orientation and measuring distances. In general, the sclera is thickest in the region of the scleral spur.

### **4.2.3 The iris**

The iris is an annulus consisting of pigmented fibro-vascular tissue known as a stroma. The stroma connects a sphincter muscle, which contracts the pupil, and a set of dialator muscles, which open it. The outer edge of the iris, known as the root, is attached to the

sclera and the anterior ciliary body (Figure 15). The iris and ciliary body converge in the region of the iris recess and insert into the scleral spur. The iris is an important anatomical feature that has a highly reflective layer on its posterior surface. The highly reflective line defines the posterior iris border and facilitates the segmentation of the anterior chamber and the extraction of the apex point. In general, a straight iris profile is seen for normal patients and its position is defined with reference to the scleral spur.

#### **4.2.4 The anterior chamber**

The anterior chamber is the space in the eye that is behind the cornea and in front of the iris (Figure 15). The anterior chamber is filled with a watery fluid known as the aqueous humor. This fluid is produced by a structure alongside the lens called the ciliary body; it passes first into the posterior chamber (between the lens and iris) and then flows forward through the pupil into the anterior chamber of the eye. The anterior chamber can be imaged from the internal cornea to the lens surface. To obtain optimal images, the ultrasound beam must be directed perpendicular to the cornea and lens interfaces. In practice, this perpendicularity is reached when maximum brightness and a clear image is projected on the screen. In general, the average axial anterior chamber depth is  $3128 \pm 372 \mu\text{m}$ .

#### **4.2.5 The trabecular-iris angle**

A cross-section through the angle region of the eye (Figure 17) shows the scleral spur, a very useful landmark for measurement that is used to maintain orientation in the angle region. In order to measure the opening angle, a point on the internal ocular wall,  $500 \mu\text{m}$

anterior to the scleral spur, is taken. In general, this point will be located on the anterior-trabecular meshwork interface. From this point, a line perpendicular to the plane of the trabecular meshwork is extended down to the opposing iris (Figure 17). The length of this line is called the angle opening distance (AOD) and is used in the angle calculation. For normal patients, the AOD is measured to be approximately  $347 \pm 181 \mu\text{m}$  when taken at  $500 \mu\text{m}$  from the scleral spur. Finally, the *opening angle* is the angle formed by the line passing through the Apex and the point on the meshwork  $500 \mu\text{m}$  from the scleral spur and the line passing through the Apex and the point obtained by the orthogonal projection (Figure 17).

# Chapter 5

## Background

This chapter discusses image processing techniques used for image enhancement and feature detection of iris ultrasound images. Many image enhancement techniques have been developed to improve the quality and appearance of images with a poor gray-scale distribution. For contrast enhancement, the simplest is a linear contrast stretch applied on the histogram of the image to make use of the entire available gray-scale range (Bovik, 2000). This will improve the visual quality of an image suffering from a narrow gray-scale distribution but it can also cause a loss of information due to clipping when pixel values are located near both extremities of the histogram. In addition, traditional edge enhancement techniques tend to amplify high-frequency noise when used to sharpen edges in an image. It is practically impossible to improve the visual quality of an image by using linear contrast stretch and edge sharpening without leading to any noise amplification. We have found the non-linear “Log-Ratio” framework of (Deng *et al*, 1994, Deng *et al*, 1993) to be a powerful collection of tools to sharpen edges and reduce noise in ultrasound images. This technique permits simultaneous edge and contrast enhancement while avoiding noise amplification, unlike classic techniques such as Unsharp Masking (Lim, 1990, Polesel *et al*, 2000). For noise reduction prior to fine enhancement, an adaptive wiener filter was implemented in order to reduce the high-frequency content in a specific neighborhood of the image. This section develops the mathematical background behind these techniques and shows its application to ultrasound images of the eye.

### 5.1 Wiener Filtering

The Wiener filter parameters are estimated from the local mean, variance and noise variance in an  $N$  by  $M$  neighborhood  $\chi$  around each pixel (Lim, 1990).

$$u(\chi_i) = \frac{1}{NM} \sum_{x,y \in \chi_i} f(x,y) \quad (12)$$

$$\sigma^2(\chi_i) = \frac{1}{NM} \sum_{x,y \in \chi} (f(x,y) - u(\chi_i))^2 \quad (13)$$

An approximation of the image noise variance  $\sigma_N^2$  is defined to be the average variance for all neighborhoods.

$$\sigma_N^2 = \frac{1}{n} \sum_{i=1}^n \sigma^2(\chi_i) \quad (14)$$

The filter is implemented in the spatial domain as follows:

$$H(x,y) = u + \frac{\sigma^2 - \sigma_N^2}{\sigma^2} (f(x,y) - u) \quad (15)$$

where  $f(x,y)$  and  $H(x,y)$  are the input and output pixels, respectively. This filter adapts to the local variance as  $\sigma^2$  is calculated for each neighborhood. Thus, if the variance is large, the filter performs little smoothing in order to preserve high frequencies or edges.

## 5.2 Linear Contrast Stretch

Linear contrast stretching methods using piecewise linear functions tend to clip the image brightness values to the gray scale range [0-255]. This can cause severe loss of information if the processed image has narrow histogram close to 0 or to 255 on the gray scale. For example, if the lowest pixel value is  $X$  and the highest is  $Y$  (Figure 18), the linear transformation on the gray-scale [0-255] values can be expressed as:

$$S X + K = 0 \quad (16.a)$$

$$S Y + K = 255 \quad (16.b)$$

where  $S$  and  $K$  are the scaling and shift operators respectively.

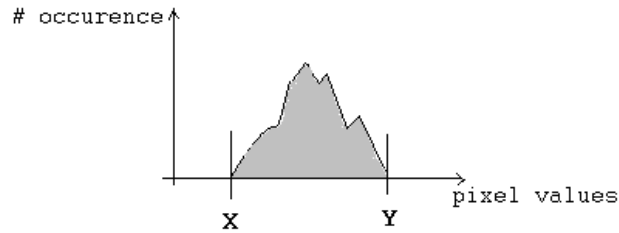


**Figure 18: Histogram of an image.  $X$  and  $Y$  correspond to the lower and higher pixel intensities.**

Solving for  $S$  and  $K$  from (16.a) and (16.b) leads to:

$$S = -\frac{K}{X} \quad (17)$$

Back in (16.b),

$$-\frac{K}{X}Y + K = 255 \quad (18)$$

The resulting linear operation can be written as:

$$\begin{aligned} r(x, y) &= S \cdot f(x, y) + K \\ &= \frac{255}{Y - X} f(x, y) - \frac{255X}{Y - X} \\ &= \frac{255}{Y - X} [f(x, y) - X] \end{aligned} \quad (19)$$

where  $f(x,y)$  and  $r(x,y)$  are the original and resulting images respectively. The technique described in section 5.4 addresses the clipping problem by non-linearly mapping the gray scale distribution of the image.

### 5.3 Linear edge enhancement

Linear edge enhancement techniques can be expressed as a space domain convolution of the image with an appropriate kernel. A well-known linear edge enhancement technique is “Unsharp Masking” (Bovik, 2000). In this method, the original image must be smoothed and then subtracted by a specific weight from the original data. Therefore, the difference between the smoothed (i.e. blurred) and the original image will give all the

fine edge details. Linear enhancement techniques generally perform well, but have severe limitations when applied on ultrasound images. Linear edge sharpening operations lead to severe noise amplification when used on poor resolution images such as in ultrasound. These edge enhancement methods suppress the variation of the overall brightness in the image while increasing the visibility of fine structures and contours. However, linear edge enhancement requires amplification of high frequency image content which necessarily amplifies image noise. In this thesis, we use a non-linear enhancement approach based on the approach of Deng et al (1995), which overcomes this problem by using the log-ratio approach and multiscale processing.

#### 5.4 Log-Ratio Approach

This section presents the log-ratio image filtering algorithm of Deng *et al* (1995). We consider the image gray level digital representation in the  $[0, M]$  range, where  $M=256$  for an 8-bit image. In order to avoid loss of information, arithmetic operations on image pixel values are defined in a logarithmically mapped space where the forward mapping function between the image pixel space ( $F$ ) and the real number space ( $\psi$ ) is:

$$\psi(F) = \log\left(\frac{(M - F)}{F}\right) \quad (20)$$

(Deng and Cahill, 1994) used the symbols  $\otimes, \oplus$  and  $\ominus$  to represent multiplication, addition and subtraction, respectively, in the log space. Figure 19 shows the logarithmic mapping function where the input pixels between  $[0, 255]$  are mapped to values between  $[-2.5, 2.5]$ . Note that as “ $F$ ” increases, the output values decrease non-linearly. This

illustrates the non-linear weighting operation performed on the input pixels of the image. Since vector addition, subtraction and multiplication are bounded operations and well defined in the log space, it is possible to derive non-linear equations that overcome the loss of information problem.

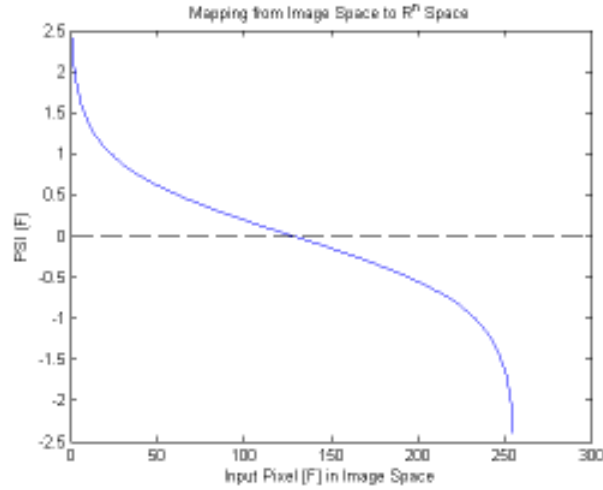


Figure 19: Log-Ratio mapping ( $M=256$ ). The x-axis represents the input pixel in Image space and the y-axis is the result obtained in the real number space.

#### 5.4.1 Addition $\oplus$ in Image Space

The addition operation in image space is defined as follows:

$$F \oplus G = \Psi^{-1}(\psi(F) + \psi(G)) \quad (21)$$

where  $G$  is the pixel gray level value in an image and  $\Psi^{-1}$  represents the inverse mapping operator. Using equation (20) for the log-ratio mapping operation, we get:

$$\begin{aligned} F \oplus G &= \Psi^{-1}\left(\log\left(\frac{M-F}{F}\right) + \log\left(\frac{M-G}{G}\right)\right) \\ &= \Psi^{-1}\left(\log\left(\frac{M-F}{F} * \frac{M-G}{G}\right)\right) \end{aligned} \quad (22)$$

If

$$z = \log\left(\frac{M-F}{F}\right) = \chi(F) \quad (23)$$

then solving for  $F$  as a function of  $z$  gives the inverse mapping from the Real Number Space to the Image Space:

$$\Psi^{-1}(z) = F = \frac{M}{10^z + 1} \quad (24)$$

Therefore,

$$\begin{aligned} F \oplus G &= \Psi^{-1}\left(\log\left(\frac{(M-F) * (M-G)}{F G}\right)\right) \\ &= \frac{M}{10^{\log\left(\frac{(M-F) * (M-G)}{F G}\right)} + 1} \\ &= \frac{M}{\left(\frac{(M-F)}{F} \frac{(M-G)}{G}\right) + 1} \end{aligned} \quad (25)$$

Figure 20 illustrates the effect of addition on the gray level range of an image in the log-ratio Space.

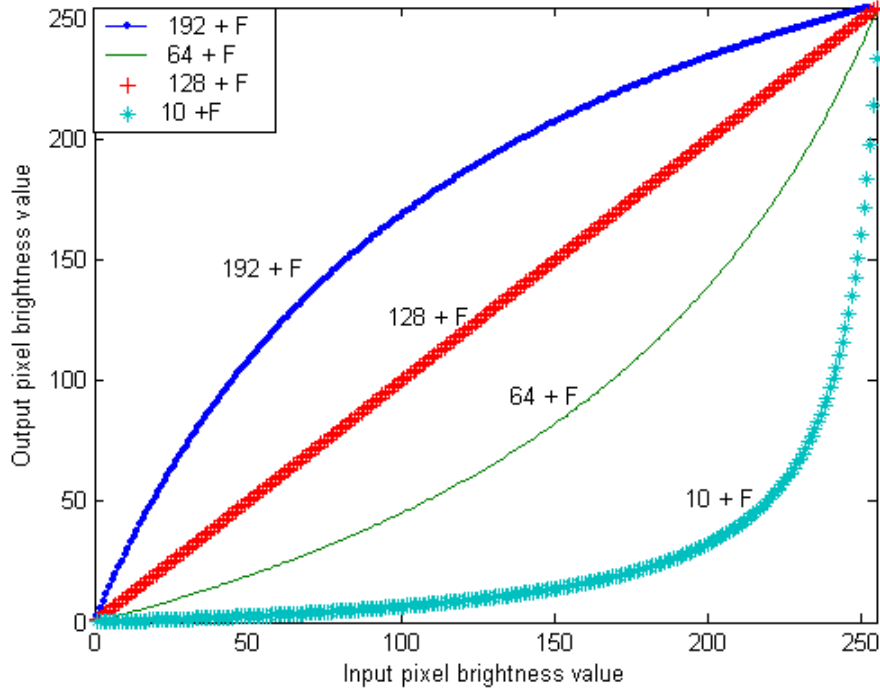


**Figure 20: Addition in log-ratio Image Space**

In Figure 20, values of 10, 64, 128 and 192 are chosen for illustrative purpose. As seen, when  $a < M/2$  (i.e.  $a=10$  or 64), the addition operation in the log-ratio space causes a non-linear expansion of the dynamic range of the bright area of an input image, resulting in a darkening effect on the image. This operation is usually applied on overexposed images where the gray level histogram of the image is stretched towards lower gray level intensity values for a better visual effect. On the other hand, when  $a > M/2$  (Figure 20, curve for  $a=192$ ), a non-linear expansion is brought on the dark area of the input image, resulting in a lightening of the gray level range. This can be used to enhance the contrast of under-exposed images. When  $M/2$  (i.e.  $a=128$ ), the addition function becomes a linear one-to-one operation. Note that the gray level of the processed image is always bounded within the  $[0,255]$  range for any ‘ $a$ ’ value.

#### 5.4.2 Multiplication $\otimes$ in Image Space

Multiplication in image space is defined as follows:

$$a \otimes F = \Psi^{-1}(a \psi(F)) \quad (26)$$

where “ $a$ ” is a real number. Using equation (20) for the log-ratio mapping, we get:

$$\begin{aligned} a \otimes F &= \Psi^{-1} \left( a * \log \left( \frac{M-F}{F} \right) \right) \\ &= \Psi^{-1} \left( \log \left[ \left( \frac{M-F}{F} \right)^a \right] \right) \end{aligned} \quad (27)$$

where,

$$a \otimes F = \frac{M}{\left( \frac{M-F}{F} \right)^a + 1} \quad (28)$$

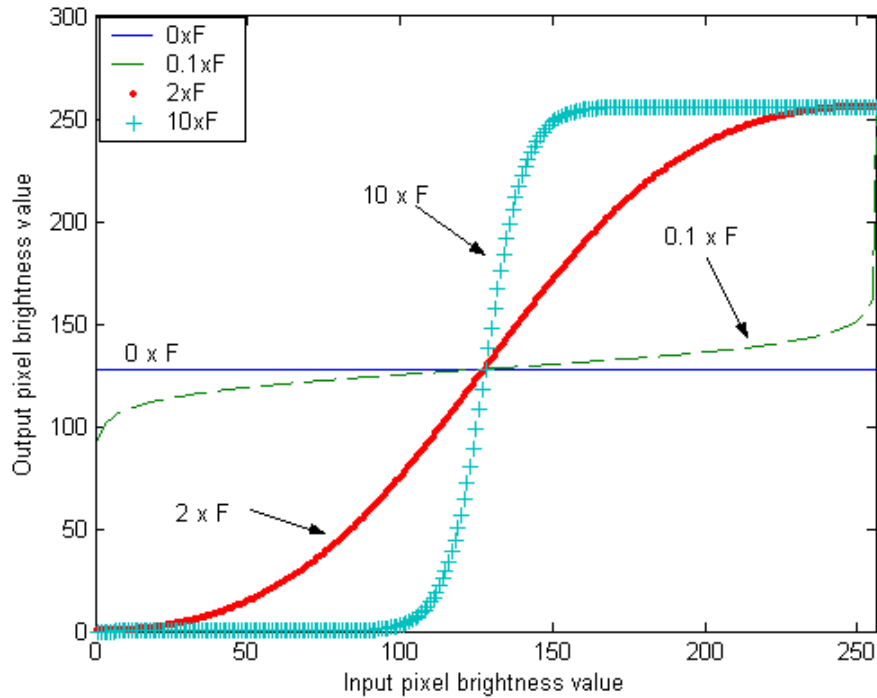


**Figure 21: Multiplication in Image Space.** The x-y axis represents the input and output pixel brightness respectively.

As seen in Figure 21, the multiplication operation in the Image Space causes a non-linear expansion of the pixel intensities in the input image. The multiplication process is again bounded to the  $[0, 255]$ . When  $a < 1$ , the pixel intensity values are mapped towards values close to  $M/2$  on the gray scale. If the scaling weight is larger than 1, but not too large (i.e.  $a=2$ ), we see a quasi-linear mapping between the input and output pixel values. However,

when  $a \gg 1$  (i.e.  $a=10$ ), the multiplication operation tends to threshold the input pixel values. In this work, the multiplication process is used to sharpen the edges in an image by amplifying its high spatial frequency information.

### 5.4.3 Subtraction $\ominus$ in Image Space

Subtraction in image space is defined as follows:

$$F \ominus G = \Psi^{-1}(\psi(F) - \psi(G)) \quad (29)$$

where  $\ominus$  is the subtraction symbol in the image space. Using equation (21) for the non-linear image mapping, we get:

$$\begin{aligned} F \ominus G &= \Psi^{-1}\left(\log\left(\frac{(M-F)}{F}\right) - \log\left(\frac{(M-G)}{G}\right)\right) \\ &= \Psi^{-1}\left(\log\left(\frac{(M-F)}{F} / \frac{(M-G)}{G}\right)\right) \end{aligned}$$

where,

$$F \ominus G = \frac{M}{\left(\frac{(M-F)}{F} / \frac{(M-G)}{G}\right) + 1} \quad (30)$$

As seen in Figure 22, the effect of vector subtraction in image space is the inverse of vector addition operation. When  $a < M/2$  (i.e. the curve labeled “10- $F$ ”), we see that most input pixels greater than  $M/2$  are mapped towards smaller values. As “ $a$ ” increases, the curves start decaying at a relatively slower rate as shown by the curve labeled “192- $F$ ” in Figure 22. Therefore, a processed image with “ $a=192$ ” will be brighter than one obtained with “ $a=10$ ”.

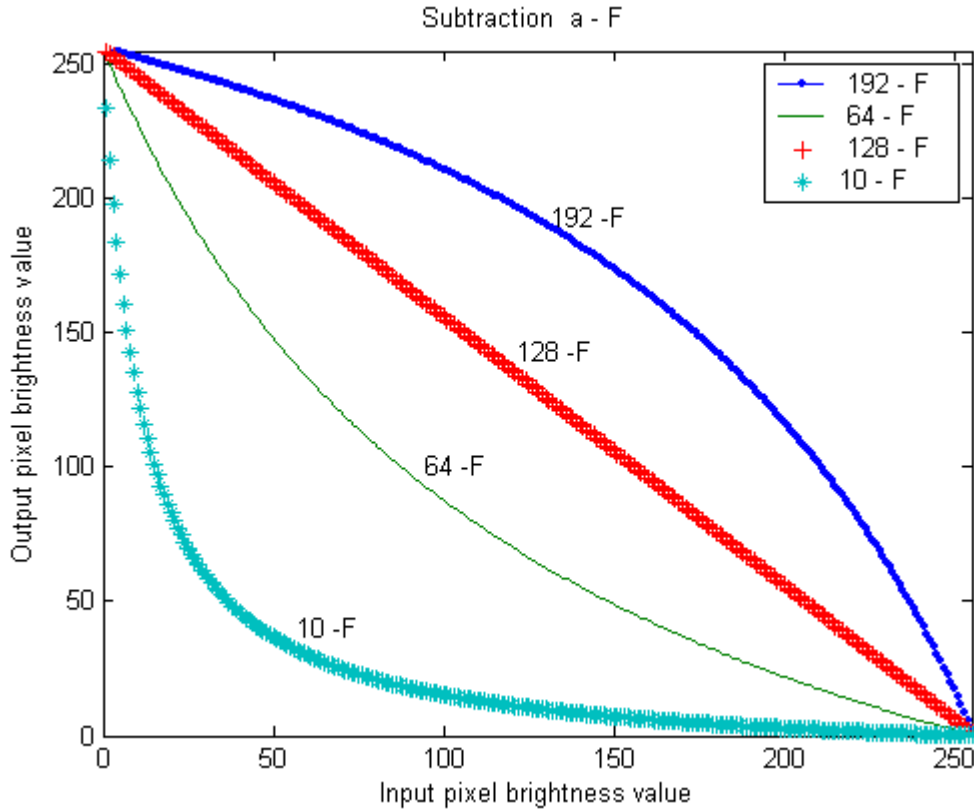


Figure 22: Subtraction in Image Space

#### 5.4.4 Non-Linear Edge & Contrast Enhancement Algorithm

The proposed algorithm in (Deng *et al*, 1994) attempts to simultaneously enhance edges and contrast in an image. For the contrast stretch, the proposed method makes use of the addition operation in the log-ratio space and for edge enhancement, the log-ratio multiplication operation used. However, the latter operation seems to amplify noise in the image. A solution to this limitation is presented in (Deng and Cahill, 1994). The main idea is to use a *multiscale* extension of expression (31) that simultaneously modifies contrast and sharpness in an image:

$$F'(x, y) = A(x, y) \oplus c \oplus \left[ s \otimes (F(x, y) \ominus A(x, y)) \right] \quad (31)$$

Controls High spatial frequencies  
and sharpness

where  $A(x,y)$ : Smoothed image  
 $c$ : parameter controlling contrast level  
 $s$ : parameter controlling sharpness level

The right hand-side of equation (31) represents high spatial frequency information of the image and is written as follows:

$$E(x, y) = (F(x, y) \ominus A(x, y)) \quad (32)$$

If the multiplication operator “ $s$ ” is applied on (32) such as:

$$E_s(x, y) = s \otimes (F(x, y) \ominus A(x, y)) \quad (33)$$

four possibilities arise:

- (i) When  $s > 1$ , the multiplication operation slightly amplifies edges in the image. This will result in an edge sharpening effect when  $E_s(x,y)$  is added to  $A(x,y)$ .
- (ii) When  $s \gg 100$ , the multiplication operation acts like a thresholding process where it classifies pixel intensities as follows:
  - a. If  $(F(x, y) \ominus A(x, y)) > M / 2 \Rightarrow E(x, y) \approx M$
  - b. If  $(F(x, y) \ominus A(x, y)) < M / 2 \Rightarrow E(x, y) \approx 0$

This can be seen in Figure 21 where the curve has an abrupt edge (i.e. step) leading to images with better edge delineation since it sets pixels either to 0 or 255. This process is similar to the unsharp mask and causes noise amplification since it also magnifies fine noise in the image.

- (iii) When  $s < 1$ , the processed image will be smoothed since high spatial frequencies are attenuated.
- (iv) When  $s=0$ , the algorithm is used only for contrast enhancement.

Furthermore, if an addition operator “ $c$ ” is combined with the smoothed image  $A(x,y)$  such as:

$$E(x, y) = c \oplus [A(x, y)] \quad (34)$$

Contrast is modified as follows:

- (i) if  $c > M/2$ , the dark area of the image will be nonlinearly expanded
- (ii) if  $c < M/2$ , the bright area of the image will be nonlinearly shifted towards the lower pixel value range of the gray scale

These operations allow simultaneous contrast and edge enhancement on an image. The remaining problem is noise amplification. To overcome this limitation, an extension to this technique is developed section 5.4.5.

#### **5.4.5 Multiscale Representation**

The image operation presented in equation (33) will tend to amplify noise if it is used to enhance edges. In order to address this issue, an algorithm based on multiple stages of equation (33) is developed, in order to suppress the noise in the processed image while enhancing edges. This is achieved through iteration where the scaling parameter must be carefully chosen in order to remove the fine texture in the processed images. This idea is illustrated in Figure 23.

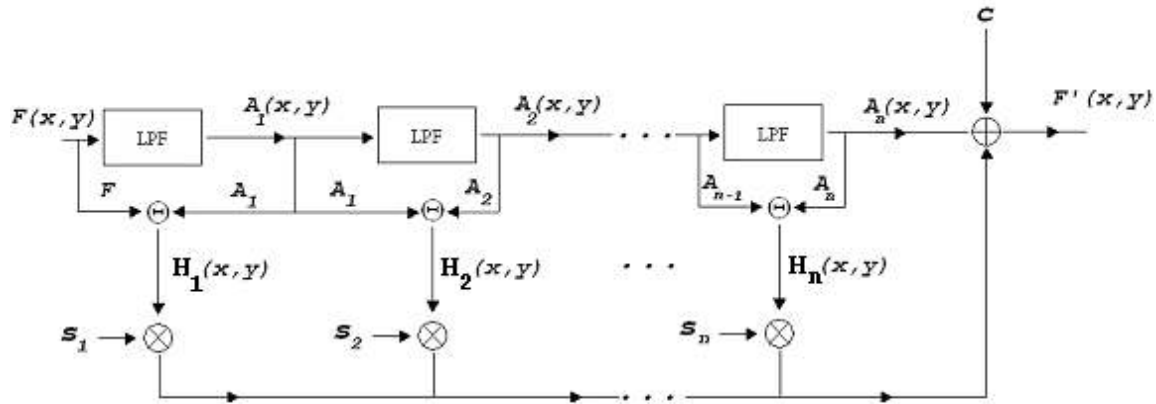


Figure 23: Multiscale Algorithm block diagram showing three stages. At each stage, the input image ( $F$  or  $A$ ) is filtered using a Gaussian [9x9] low-pass filter. An image containing only high-frequencies  $H(x,y)$  is obtained by subtracting the smoothed output from the input. The edge amplification parameter  $s_i$  is selected at each stage,  $i$ , based on the level of high frequency noise in  $H_i(x,y)$  as described in section 5.4.5.  $c$  is a scalar controlling the contrast level in the enhanced image. All operations are defined in the logarithmic mapping space. The algorithm is repeated for  $n$  iterations until  $A_{n-1}(x, y) \ominus A_n(x, y) \approx 0$ .

The number of iterations  $n$  depends on the high spatial frequency content of the image.

After a certain number of iterations, the difference between two successive smoothed

images will become very small ( $A_{n-1}(x, y) \ominus A_n(x, y) \approx 0$ ) which implies that  $s_i$  can be set

to a value greater than one, and the algorithm can terminate when desirable edge

enhancement level is achieved (Figure 24). The enhanced image computed by the

algorithm is a quasi-binary image when  $s \gg 100$ , which facilitates the selection of a

threshold at the binarization process. An example of simultaneous contrast and edge

enhancement can be seen in Figure 24 and Figure 25 where a section of the ultrasound

image of the eye is processed by the multiscale algorithm. This is achieved through

selection of the scaling parameters “ $s$ ”.  $s_i$  is set to a value  $< 1$  for the first stages to smooth

high frequency noise. In stages after noise is sufficiently reduced,  $s_i$  is set to a value  $> 1$  to

amplify edges and contours. Figure 25 shows representative images of the effect of

values of  $s$ . For example, Figure 25(b) illustrates an inadequate selection of the

parameters (all  $s_i > 1$ ) resulting in significant noise amplification, while Figure 25 (c) shows the output when the parameter values are adequately selected.

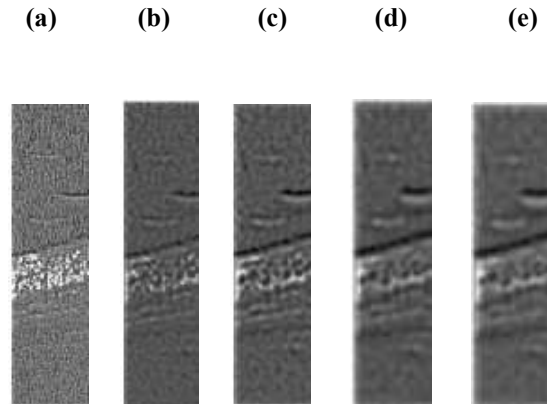
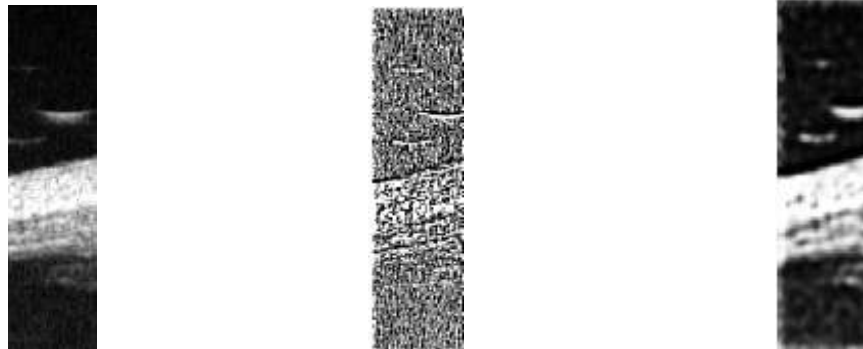


**Figure 24:** A vertical section of representative images,  $H_i$ , obtained as a result of the subtraction operation  $(A_{n-1}(x,y) \ominus A_n(x,y))$  in the multiscale algorithm for 5 iterations. (a) represents a cropped section of the processed image after the first iteration and (e) after 5 iterations.



(a) Original image

(b)  $s_i > 1$

(c)  $s_1, s_2, s_3 < 1$  and  $s_4, s_5 > 1$

**Figure 25:** Vertical sections of a sample image to illustrate parameter selection in the multiscale algorithm

# Chapter 6

## Algorithm design

Chapter 5 introduced image enhancement techniques that used for edge and contrast enhancement in UBM images of the eye. This chapter develops an algorithm to automate the measurement of the location of clinically relevant features in ultrasound images of the eye. A part of this work has been submitted for publication in the Transactions on Medical Imaging (Youmaran, Dicorato, Munger, Hall and Adler, 2005). The proposed algorithm is designed to calculate two clinical parameters, the *open-angle* and *AOD* as shown in Figure 17 and defined in (Nishijima *et al*, 2000, Pavlin *et al*, 1991, American Academy of Ophthalmology, 2000). In performing this calculation, it must delineate the sclera, and locate the scleral spur, the trabecular-iris recess, and the anterior chamber. The algorithm is structured into three steps, as shown in Figure 27: steps 1 and 2 are executed independently and the result merged into step 3 to complete the feature extraction and resultant calculations.

### 6.1 Step 1: Coarse enhancement

The goal of this section is to extract from the image the anterior chamber region. The sequences of operations are described in the flowchart given in Figure 27. A speed of sound in tissue of 1530 m/s was used to convert time into distance when constructing ultrasound images of the eye (Pavlin, 1993). The imaged area section on the operating

screen of the UBM machine is 5mm x 5mm (Pavlin, 1995). Images are 256x256 pixels which lead to image operations based on rectangular pixels of  $19.5 \mu\text{m} \times 19.5 \mu\text{m}$ .

### 6.1.1 Image thresholding

An intensity threshold, THR, is selected based on a subset of images of the anterior chamber region cropped manually. THR is selected at the tail of the histogram for the anterior chamber region (Figure 26). Once obtained, THR is fixed for all scanned images. Pixels with intensity above THR are set to 255; otherwise, the value is unchanged. The thresholded image is denoted as  $f_{th1}$ .

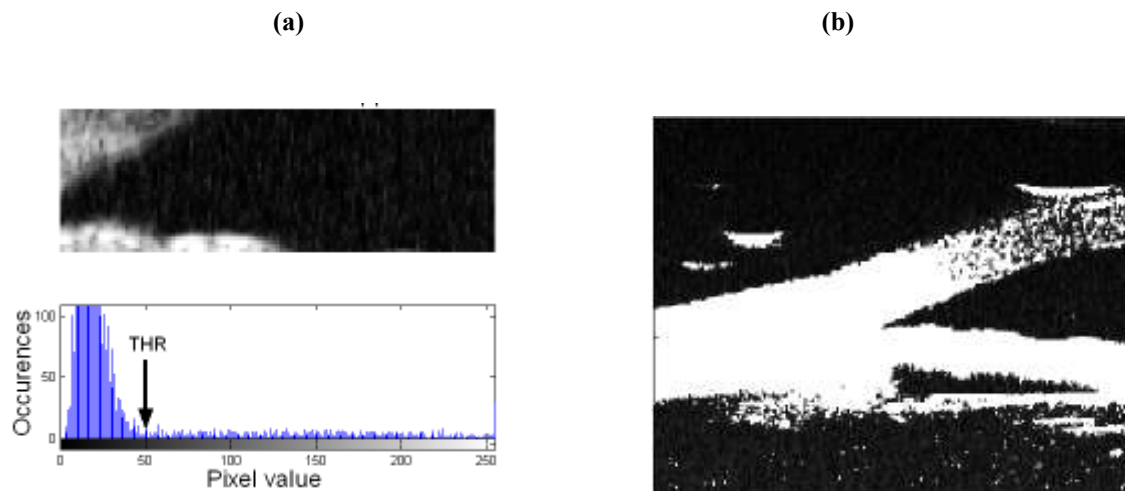


Figure 26: (a) Threshold (THR) selection based on the histogram of a cropped anterior chamber region (b) Thresholded image showing better edge delineation in the anterior chamber region

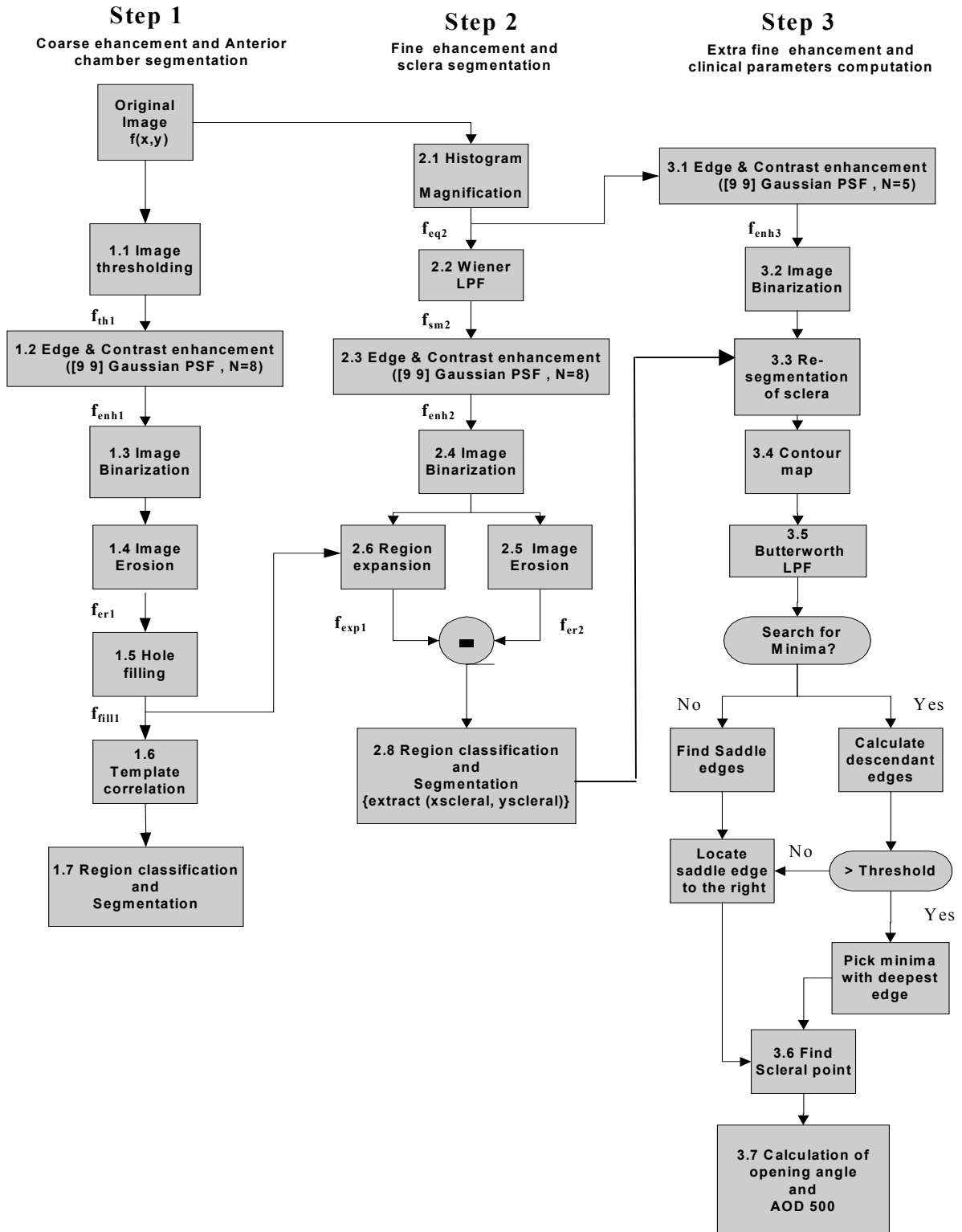


Figure 27: Flowchart illustrating algorithmic steps. The algorithm is divided in 3 steps. Step 1 describes steps to segment the anterior chamber. Step 2 for sclera region extraction and scleral spur identification. Step 3 for verification and clinical parameters computation.

### 6.1.2 Non-Linear Edge & Contrast Enhancement

$f_{th1}$  is low pass filtered with a 9x9 Gaussian filter with  $N=8$  iterations, using the non-linear edge and contrast enhancement algorithm described in section 5.4.4. The output of this system results in a coarsely enhanced image  $f_{enh1}$  with reduced noise and high-frequencies content.



Figure 28: Coarsely enhanced quasi-binary ultrasound image of the eye using the Non-Linear Edge & Contrast Enhancement algorithm

### 6.1.3 Image Binarization

Using the grayscale threshold,  $THR$ , the coarsely enhanced image ( $f_{enh1}$ ) pixels are binarized (Figure 29).



Figure 29: Coarsely enhanced binary image

#### 6.1.4 Image erosion

Erosion is applied on the binary image to remove spurious features. A 5x5 square-shaped structuring element is used for the erosion process. The resultant image is denoted by “ $f_{er1}$ ”.



Figure 30: Light erosion applied on the enhanced image to reduce artifacts

#### 6.1.5 Hole Filling

Small openings (holes) in the trabecular meshwork and the iris are detected and filled. The filling operation is performed by first finding all connected background regions

(white pixels) in the binary image and then, by setting pixel values to zero (black). The filled image 'f<sub>fill</sub>' is later used for correlation with a template image of the anterior chamber.



**Figure 31: Image with all holes filled to facilitate the segmentation process of the anterior chamber**

### 6.1.6 Template Correlation

The anterior chamber is a large and roughly triangular feature, and can thus be identified using correlation with an appropriate template. In order to compensate for variability in the shape of this region, 3 template regions were chosen from representative image (Figure 32) of subjects with different degrees of glaucoma.



**Figure 32: Template images used for the correlation process for the detection of the anterior chamber. Each image is of different size and shape to represent the variability of the degree of glaucoma.**

The enhanced image is then correlated with each template and the average correlation point  $(x_c, y_c)$  computed from the mean of all maximum correlation points.

### 6.1.7 Anterior Chamber Classification and Segmentation

Each closed region in “ $f_{fill}$ ” is analyzed to identify the most likely to be the anterior chamber. Classification is based on the geometrical properties: object area, centroid, major-axis and minor-axis length (using an elliptical model). The following parameters are computed for segmentation of each closed region:

- (a) Center: Defined as the center coordinate of a region
- (b) Distance from maximum correlation point  $(x_c, y_c)$ : Defined as the distance between the calculated center in (a) and the average correlation point  $(x_c, y_c)$  computed in section 6.1.6.
- (c) Area: Defined as the total number of pixels characterizing a closed region.

The regions that meet the following requirements are to be considered as candidates in the segmentation process.

- (i) Area  $> 50$  pixels; otherwise, the region is considered to be noise.
- (ii) The distance between the center of the closed region and  $(x_c, y_c)$  must be minimum; ideally zero.

If more than one region has the same minimum distance, then the selection is based on the maximum area. Once the anterior chamber is segmented (Figure 33), the upper and lower edge coordinates are extracted. Also, the apex point  $(x_{apex}, y_{apex})$  is defined by locating the black pixel that is the most to the left of the anterior chamber as shown in

Figure 17. If no regions are detected, the algorithm terminates since the coordinates of the anterior chamber cannot be calculated.



**Figure 33: Segmented anterior chamber**

## **6.2 STEP 2: Fine enhancement**

The goal of this section of the algorithm is to identify the sclera region. The algorithm is shown in (Figure 27).

### **6.2.1 Histogram magnification**

A histogram magnification (Figure 34) is applied to enhance the texture of interest. Threshold values are calculated corresponding to  $t_L=15\%$  and  $t_H =85\%$  of the total number of pixels in the histogram. Image normalization is applied using the following equation:

$$F'(x, y) = (F(x, y) - t_L) \left( \frac{255}{t_H - t_L} \right) \quad (35)$$

where  $F(x,y)$  and  $F'(x,y)$  are the input and output pixels, respectively. The thresholded image (Figure 35) shows better contrast and edge delineation around the sclera region.

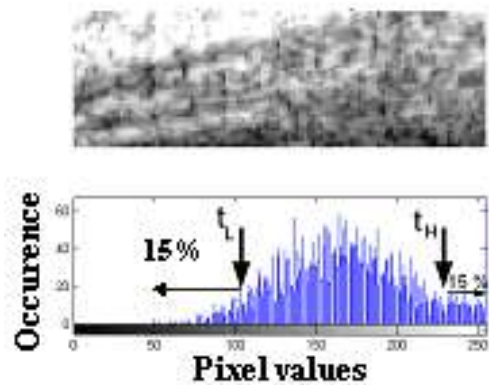


**Figure 34: Cropped Sclera Region & its corresponding histogram. The upper and lower thresholds are depicted on the histogram**

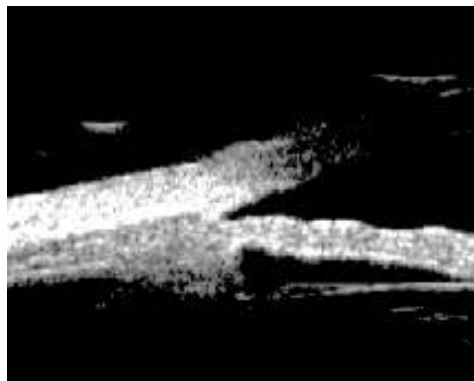


**Figure 35: Thresholded image showing an enhanced sclera region with better contrast**

### 6.2.2 Wiener Filtering

The image is filtered using an adaptive Wiener filter (Lim, 1990, Polesel *et al*, 2000) with a 9x9 pixel neighborhood. The purpose of this filter is to reduce high-frequencies for different neighborhoods in the image prior to fine enhancement.



**Figure 36: Wiener filtering to reduce noise in the sclera region**

### **6.2.3 Non-linear Edge & Contrast Enhancement**

Image is obtained using the same process as in section 6.1.2. The finely enhanced image (Figure 37) contains the sclera region (circled) that is used to extract the scleral spur.

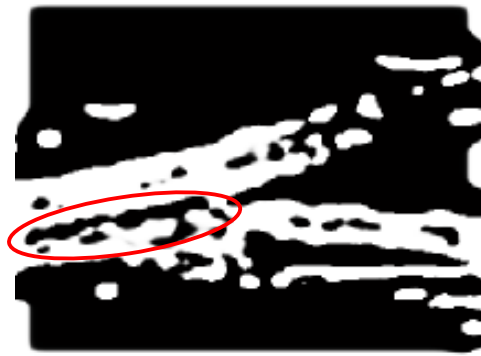


**Figure 37: Finely enhanced image**

### **6.2.4 Image Binarization**

The finely enhanced binary image is obtained using the same process and thresholds as in section 6.1.3.

### 6.2.5 Image Erosion

Iterative erosion is repeated for  $n=4$  times to remove artifacts in the enhanced binary images. The classic  $3 \times 3$  erosion operator is modified in order to preserve weak edges, as follows: the center pixel (located at  $(0,0)$ ) is set to background if and only if both adjacent (horizontal or vertical) pixels are background. The resultant image is denoted by “ $f_{er2}$ ”.

### 6.2.6 Region expansion

“ $f_{fill}$ ” is dilated with a circular-shaped structuring element of size 5 (Figure 38). This enlarges all regions in the image denoted by “ $f_{exp1}$ ”, which is used for the subtraction process described in the section 6.2.7.

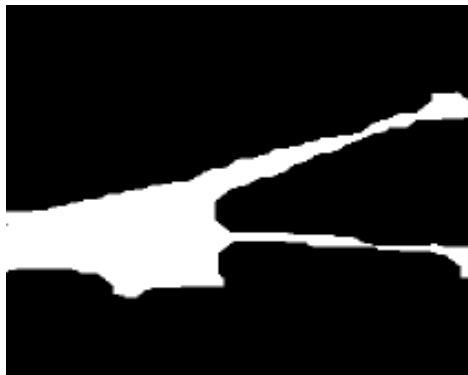


Figure 38: Coarsely enhanced image expanded prior to subtraction

### 6.2.7 Region subtraction

The expanded image (coarsely enhanced) “ $f_{exp1}$ ” is subtracted from the eroded image (finely enhanced) “ $f_{er2}$ ”. This procedure removes all large regions in the image and keeps only the fine details of interest (Figure 39).



**Figure 39: Resulting image after subtraction. Only fine details of interest remain in the image**

### 6.2.8 Sclera region classification and segmentation

For segmentation of the sclera region, the following parameters are computed:

- (a) Boundary pixels coordinate: the pixel that is furthest to the right and is located within each of the closed regions ( $x_{\text{right}}, y_{\text{right}}$ )
- (b) Distance from the apex point ( $x_{\text{apex}}, y_{\text{apex}}$ ) of the anterior chamber to ( $x_{\text{right}}, y_{\text{right}}$ ) of each classified region
- (c) Area in pixels of each region
- (d) Major axis length of the closed regions

In order to segment the sclera from all possible regions in the enhanced image, each closed region is analyzed independently. By first scanning through the processed image, any region with an area less than 50 pixels is rejected since it is considered to be speckle noise or too small to be a proper sclera region candidate. Afterwards, the distance between ( $x_{\text{right}}, y_{\text{right}}$ ) and ( $x_{\text{apex}}, y_{\text{apex}}$ ) is calculated for the remaining regions with area greater than 50 and the region that has the smallest distance is considered to be the sclera.

If multiple regions have the same minimum distance, then the selection is based on the area and the major-axis length, based on observed ultrasound images of the eye. Once the sclera is segmented, its center  $(x_{scleral}, y_{scleral})$  as well as its upper edge coordinates are extracted.



**Figure 40: Segmented sclera region**

### **6.3 STEP 3: Extra fine enhancement**

The goal of this section is to improve the robustness of the detection by applying extra fine enhancement to the original image and re-extracting a new sclera region. If the newly extracted scleral spur coordinates correlate with the ones previously calculated, then the remaining clinical parameters can be computed; otherwise, the sclera region cannot be segmented, and the algorithm terminates.

#### **6.3.1 Non-Linear Edge & Contrast Enhancement**

The enhancement algorithm (section 5.4.5) is applied to  $f_{eq2}$  computed in section 6.2.1. In order to achieve fine enhancement, fewer iterations ( $n=5$ ) are used, resulting in a significant reduction of the blur. The enhanced image is denoted as “ $f_{enh3}$ ”.



Figure 41: Extra finely enhanced image showing the sclera region with a clean contour

### 6.3.2 Image Binarization

This procedure is the same as the one mentioned in section 6.2.4.

### 6.3.3 Sclera region Classification and Segmentation

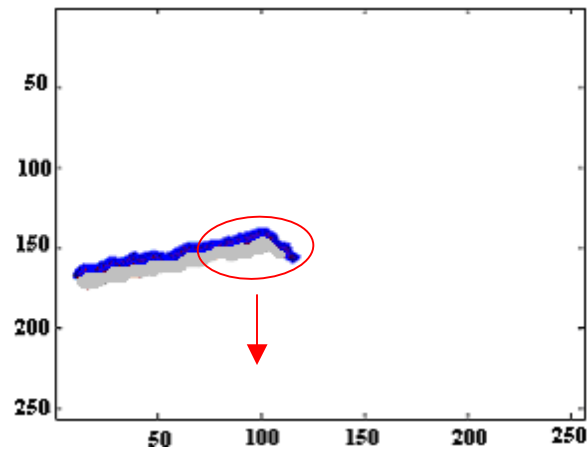
The approach of section 6.2.8 is used except an additional parameter is used to account for the distance ( $d_{c-sc}$ ) between the center of each detected candidate region and  $(x_{scleral}, y_{scleral})$ . A region is classified as the best sclera candidate if it passes all the requirements of section 6.2.8 and has the smallest  $d_{c-sc}$ .



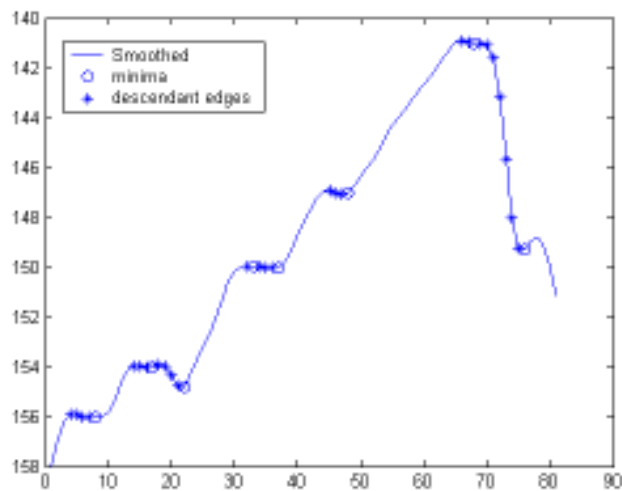
Figure 42: Extra finely enhanced sclera region segmented

### 6.3.4 Sclera Contour Mapping

Once the sclera has been identified (Figure 43 a), the scleral spur is located based on signal processing on the outline of the top boundary of the extracted sclera region. This outline is determined by scanning the image vertically and determining the uppermost location of the pixels on the sclera image (Figure 43 b).



(a)



(b)

Figure 43: (a) sclera region with outline mapped onto segmented region, (b) Plot of cropped desired outline (right half section of the sclera outline) showing minima and descendant edges sample points on the smoothed sclera contour. The x-y axes are the spatial coordinates of the image. The x-axis of the cropped outline in (b) represents the number of sample points in the image.

### 6.3.5 Sclera Contour Smoothing Filter Design

A non-recursive 4th order Butterworth smoothing filter, with normalized cutoff frequency ( $w_c$ ) of 0.45, is used to remove outliers and abrupt variations (fluctuations) in the outline that may result from poor resolution and image noise. The filtered data set is defined as  $F_{\text{filt}}(x)$ . The value of the normalized cutoff frequency was manually tuned to provide a compromise in terms shape fidelity to the shape and rejection of unwanted saddle points. Since we know that the scleral spur is located to the right of the sclera region, only the right-half side of the data points on the sclera contour is searched. This truncation of the size of the detected outline reduces the search time. This new array of data is denoted as “ $F_{\text{trunc}}(x)$ ”.

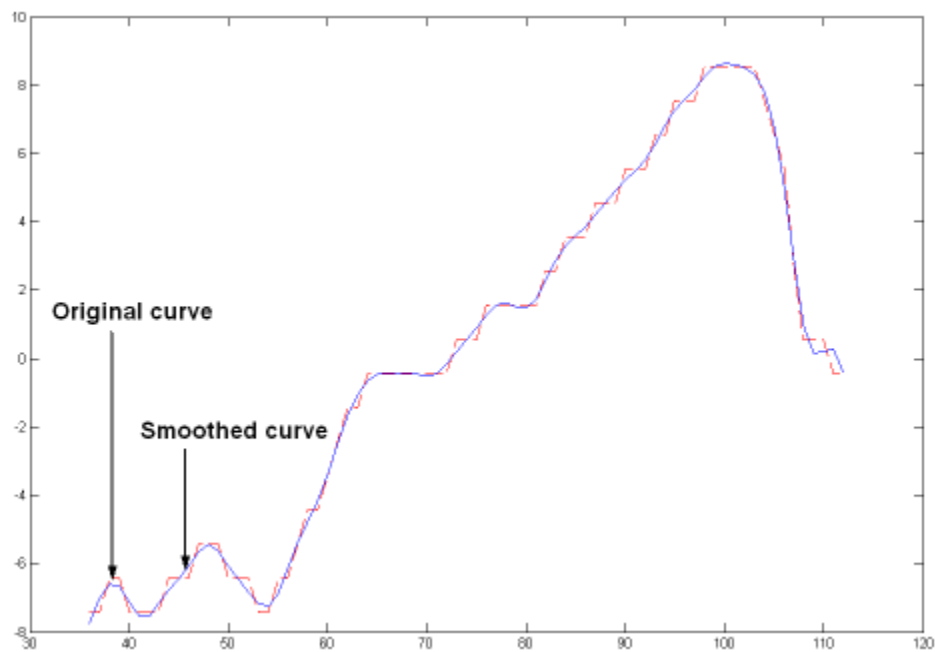


**Figure 44: Smoothed sclera contour using the Butterworth LPF filter. The x-y axes are the spatial coordinates of the image.**

### 6.3.6 Scleral Spur Detection

The scleral spur is detected by first applying a gradient operator on  $F_{\text{trunc}}(x)$  (Figure 43 b) and then computing all minima coordinates as well as the points along the descendent edge prior to each local minimum. If no minima are detected, all points with zero gradients are located and defined as saddle edges.

*Identification/detection of the scleral spur is completed when one of the following occurs:*

If one local minimum is found, then this point becomes the scleral spur coordinate. If multiple minima are located on  $F_{\text{trunc}}(x)$ , then all points along the descendant edges are used in order to calculate the magnitude of each edge ( $\Delta_{\text{edge}}$ ) prior to a minimum. For each descendent edge found within the outline  $F_{\text{trunc}}(x)$ ,  $\Delta_{\text{edge}}$  is computed as the difference between the maximum pixel value and the minimum pixel value along that edge. The descendant edge with the largest ( $\Delta_{\text{edge}}$ ) symbolizing the deepest dip is chosen as the scleral spur coordinate. On the other hand, if no minima are found along the contour, then saddle edges are used since they represent possible locations of the scleral spur on the sclera contour. Knowing a priori that the scleral spur occurs to the right side of the contour, the saddle edge located most to the right of the 1-D outline is selected as the scleral spur coordinate. The scleral spur coordinate is denoted as  $(x_s, y_s)$ .

### 6.3.7 Determination of Measured Parameters for Glaucoma

This section describes calculation of: (1) open-angle; and (2) angle-open distance (AOD), as shown in Figure 17. These parameters require the location of the apex point previously computed in section 6.1.7. This location will be used to define the angle.

*AOD 500 & Open-Angle Calculation:* The AOD 500 is measured along an orthogonal projection from the trabecular meshwork to the iris (Nishijima *et al*, 2000, Pavlin *et al*, 1991), as illustrated in Figure 17. Its calculation requires the computation of:

- 1) The contour along the upper half of the anterior chamber from the scleral spur to the upper vertex
- 2) The contour from the scleral spur along the iris on the lower anterior chamber to the lower vertex. The lower contour on the processed (enhanced) image is shifted from its original location due to the blur introduced by the multiscale processing. To correct the offset imposed by the blur, we recalculate a new contour using the original image. Starting at the offset pixel position (black pixel within the anterior chamber), scan vertically in the downward direction for the first pixel that is different from black. This is shown in Figure 45.

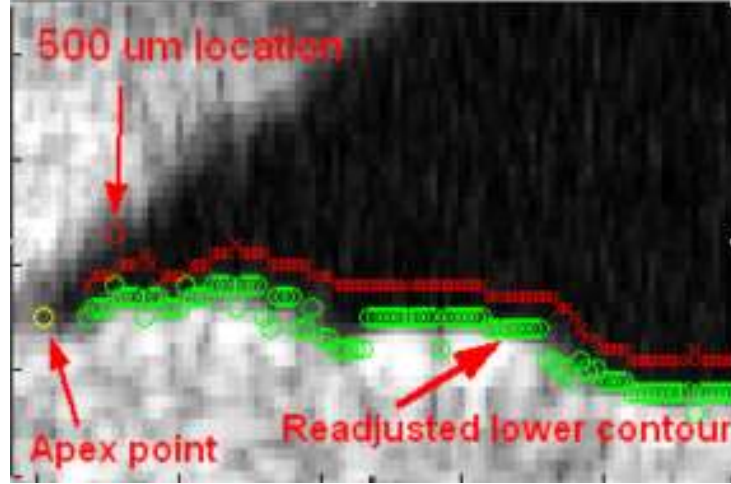


Figure 45: Lower contour of the iris re-adjusted

3) The location  $500 \mu\text{m}$  from the scleral spur along the contour on the trabecular meshwork is computed (Figure 46) as follows:

$$\phi = \tan^{-1}\left(\frac{h}{d}\right) \quad (36)$$

$$y_{500} = y_s + 25 \times \cos \phi \quad (37)$$

$$x_{500} = x_s - 25 \times \sin \phi \quad (38)$$

where  $h = x_s - x_{\min}$  and  $d = y_{\min} - y_s$

The measured contours provide data for the orthogonal projection calculation between the two segments of the eye. By calculating the inner product between the vectors defined as:

$$\vec{v}_1 = \{(x_{500} - x_{apex}), (y_{500} - y_{apex})\} \quad (39)$$

$$\vec{v}_2(n) = \{(x_{lower}(n) - x_{500}), (y_{lower}(n) - y_{500})\} \quad (40)$$

we can find the orthogonal projection coordinate along the lower iris trace.  $n$  represents the sample points of the lower iris contour. Denoting this location as  $(x_{low\_mid}, y_{low\_mid})$  and computing the vector

$$\vec{v}_3 = \{(x_{low\_mid} - x_{apex}), (y_{low\_mid} - y_{apex})\} \quad (41)$$

leads to the calculation of both the AOD 500 and the open-angle. The calculation of the AOD 500 length, in  $\mu\text{m}$ , is given by:

$$\vec{d}_{AOD500} = \eta_{conv} \sqrt{(x_{500} - x_{low\_mid})^2 + (y_{500} - y_{low\_mid})^2} \quad (42)$$

where  $\eta_{conv} = 19.5 \mu\text{m}/\text{pixel}$  is the resolution of the ultrasound system used.

If the 500  $\mu\text{m}$  coordinate location appears to the left of the  $(x_{apex}, y_{apex})$  point, then the open-angle is  $0^\circ$ . Otherwise, an open-angle, in radians, is calculated as:

$$\theta = \cos^{-1} \left( \frac{|\vec{v}_1 * \vec{v}_3|}{|\vec{v}_1| |\vec{v}_3|} \right) \quad (43)$$

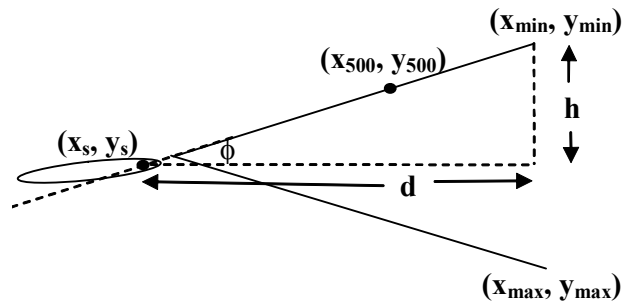


Figure 46: AOD 500 Calculation Diagram



**Figure 47: Original image showing the computed clinical parameters of interest. The blue dot indicates the scleral spur location, the yellow is the apex point and the red dots show the 500um point and its orthogonal projection respectively.**

# Chapter 7

## Results

Ultrasound images are obtained from patients at the University of Ottawa Eye Institute using the UBM System Model 840 (Zeiss-Humphrey), using the protocol described in (Daneshvar *et al*, 2000). The data used within the study was taken from patients who had been diagnosed with glaucoma. The data was used initially in the study of pseudoexfoliation syndrome (Damji *et al*, 1998). The patient's data was then used later for this study. Patient selection was based on: 1) diagnosis of glaucoma in the patient, or 2) genetic susceptibility to the disease as indicated by its presence in their family. In total, 80 patients were enrolled in previous study. For this present work, one image was taken for each patient (in order to ensure statistical independence of results) resulting in 80 images to be analyzed. Each patient was placed on a reclining chair with a headrest and an apparatus was placed surrounding the eye allowing a transducer to be placed on the ocular region. The transducer is scanned in distinct directions in order to extract the appropriate ultrasound image on the screen visible to the operator. The images are then stored on the local hard disk in PCX format. As described by Deepak (2002), the technologist manually identifies the location of the clinical features on the screen. The AOD 500 is then calculated and the open-angle is measured with a protractor centered at the apex point of the anterior chamber (Pavlin *et al*, 1991).

Using the algorithm described in this thesis, 80 different images were processed on a 2.4 GHz Intel Pentium III processor with 512 MB of SDRAM. The algorithm was implemented in Matlab and the execution time for one image is 32 seconds.

In section 6.1.1, a threshold (THR) of 50 was used. In section 6.1.2, the s-parameters were set to  $s_{1,2,3,4}=0.1$  and  $s_{5,6,7,8} = 20$  for 8 iterations. In section 6.2.1, the lower and upper thresholds are calculated to be 85 and 220, respectively. Figure 47 illustrates all calculated clinical features of interest using this algorithm. By treating the technologist-identified parameters as gold standards, we estimated the detection position (offset) error of the algorithm. The offset error histograms are shown in Figure 48. Overall, the offset error was smaller in the vertical direction compared to the horizontal direction. In the horizontal direction, the mean error is 2 pixels (39.5  $\mu\text{m}$ ) toward the eye centre and standard deviation is calculated to 6.7 pixels (130.65  $\mu\text{m}$ ). In the vertical direction, the mean error is 1.42 pixels (27.69  $\mu\text{m}$ ) toward the back of the eye with a standard deviation of 2.71 pixels (52.8 $\mu\text{m}$ ).

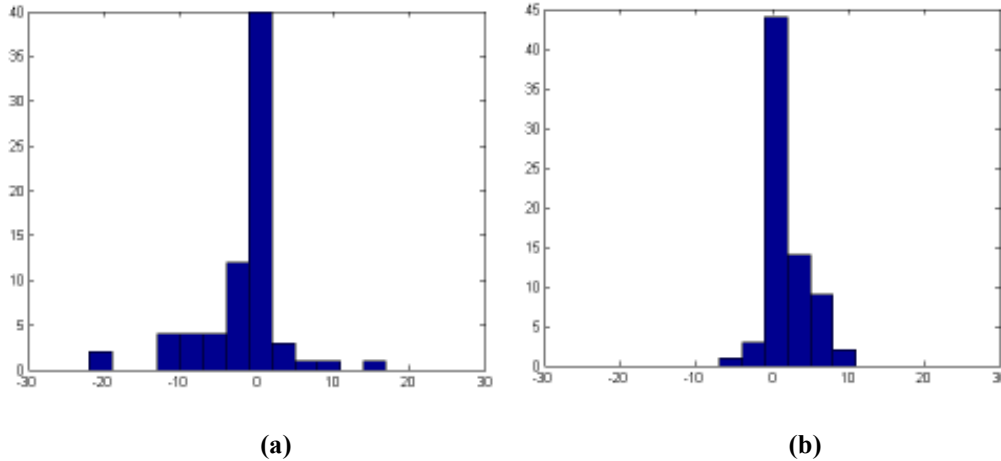


**Figure 48: Offset pixel error histogram in the (a) horizontal direction  $\mu_H=-2$ ,  $\sigma_H=6.7$  pixels, (b) vertical direction  $\mu_V=1.42$ ,  $\sigma_V=2.71$  pixels. The x and y axis represent the pixel offset error and occurrences, respectively.**

The developed algorithm can generate three possible outcomes. If the algorithm fails to segment the regions of interest or cannot process a specific image, the clinical parameters are not computed (outcome 1). Otherwise, clinical parameters are computed. If the calculated parameters differ from those measured by the technologist within  $97.5 \mu\text{m}$  (5 pixels), the output is considered a success (outcome 2). Otherwise, the offset error is greater than  $97.5 \mu\text{m}$  (5 pixels) in both direction and the algorithm fails (outcome 3). Based on the outcomes described above, in 5% of cases, the algorithm could not analyze the images (outcome 1). In the remaining cases where clinical parameters are computed, features were correctly identified in 97% of images (outcome 2). Thus, 3% of images presented inaccurate estimates (outcome 3) of the clinical parameters, with  $351\mu\text{m}$  (18 pixels) offset error average.

### 7.1 An example of Outcome 1

This example illustrates a case where the segmentation of the sclera region failed causing errors in the calculation of the scleral spur coordinates. Figure 49 (a) represents a severe

case of Glaucoma where the scleral spur is located far ( $>1000\mu\text{m}$ ) from the Apex point. The trabecular-iris angle is closed or zero since the  $500\ \mu\text{m}$  point from the scleral spur is located to the left of the Apex point (Figure 49 (a)). As seen in Figure 49 (c,d), region 2 is chosen to be the sclera region since  $d_2$  is smaller than  $d_1$  and satisfies the classification process where  $d_i$  is the distance between the Apex point and the right-most pixel value in candidate region  $i$ .

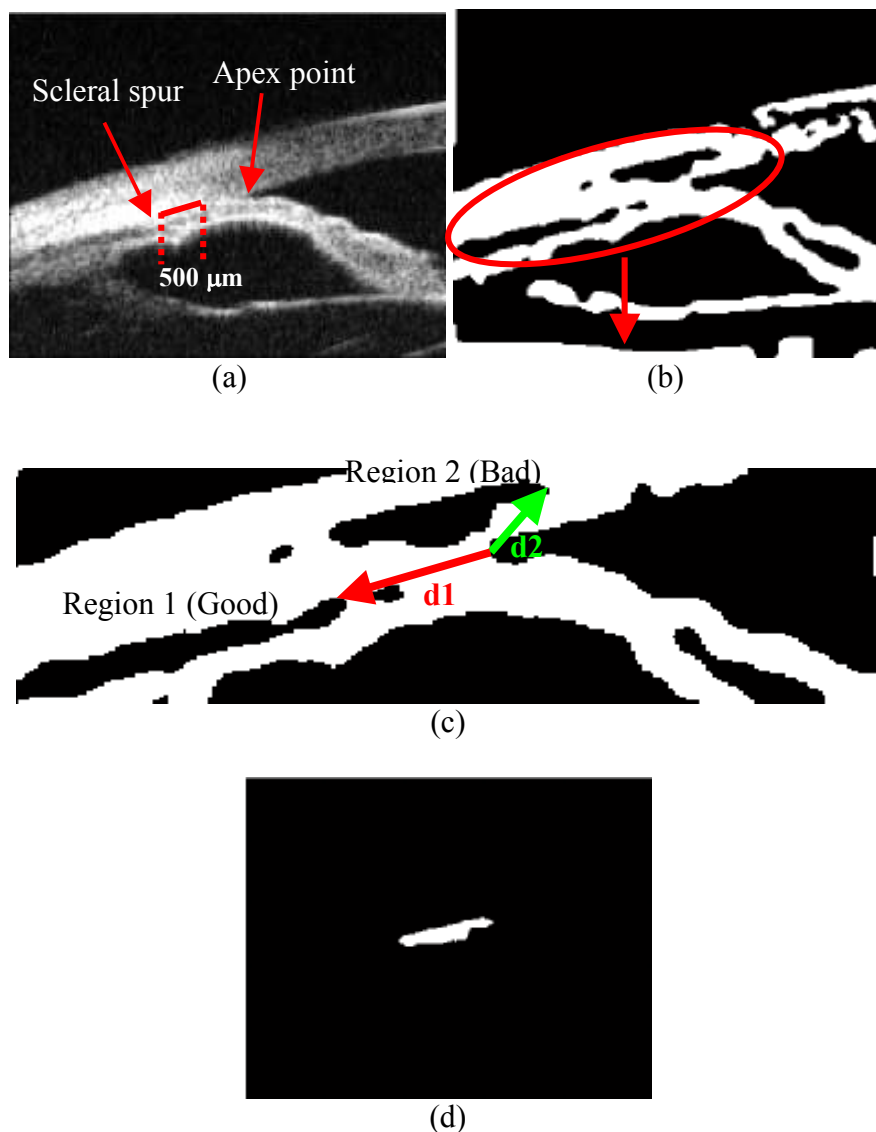


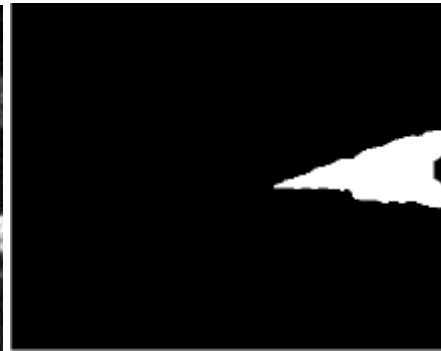
**Figure 49: Example of an outcome 1 (Segmentation failed) where (a) Original image, (b) Coarsely enhanced image, (c)  $d_2 < d_1$  which satisfies the classification procedure and results in the rejection of the sclera region, (d) Segmentation of the sclera region failed**

## 7.2 An example of Outcome 2

This example illustrates a case where the segmentation of the sclera region succeeded and all clinical parameters computed with zero offset error compared to the technologist observation. From the extracted scleral spur coordinates (Figure 50 (e)), a trabecular-iris angle of  $31.6^\circ$  and an AOD distance of  $175.5 \mu\text{m}$  are computed.



(a)



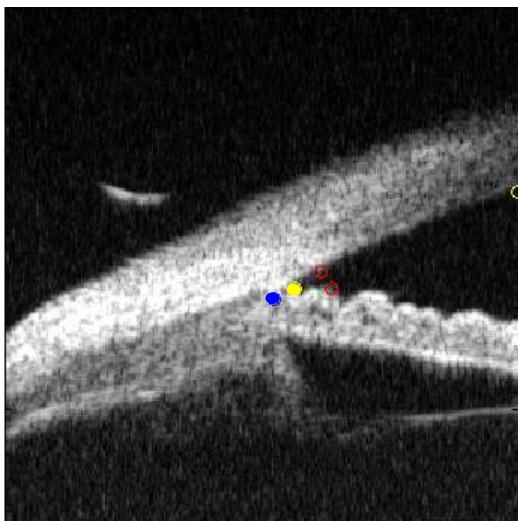
(b)



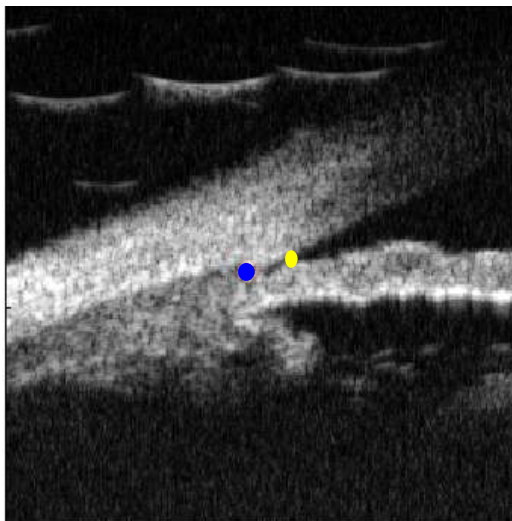
(c)



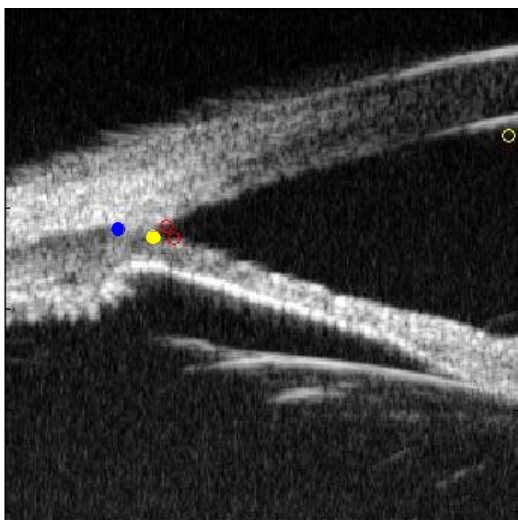
(d)



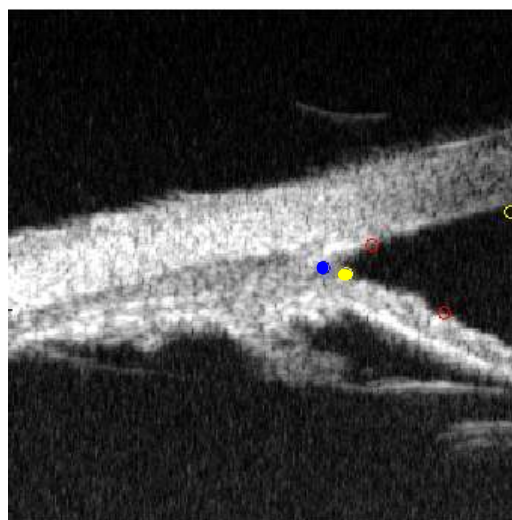
$\theta=31.6^\circ$ , AOD=175.5  $\mu\text{m}$



$\theta=0^\circ$ , AOD=0  $\mu\text{m}$



$\theta=40.7^\circ$ , AOD=140.4  $\mu\text{m}$



$\theta=68^\circ$ , AOD=951.6  $\mu\text{m}$

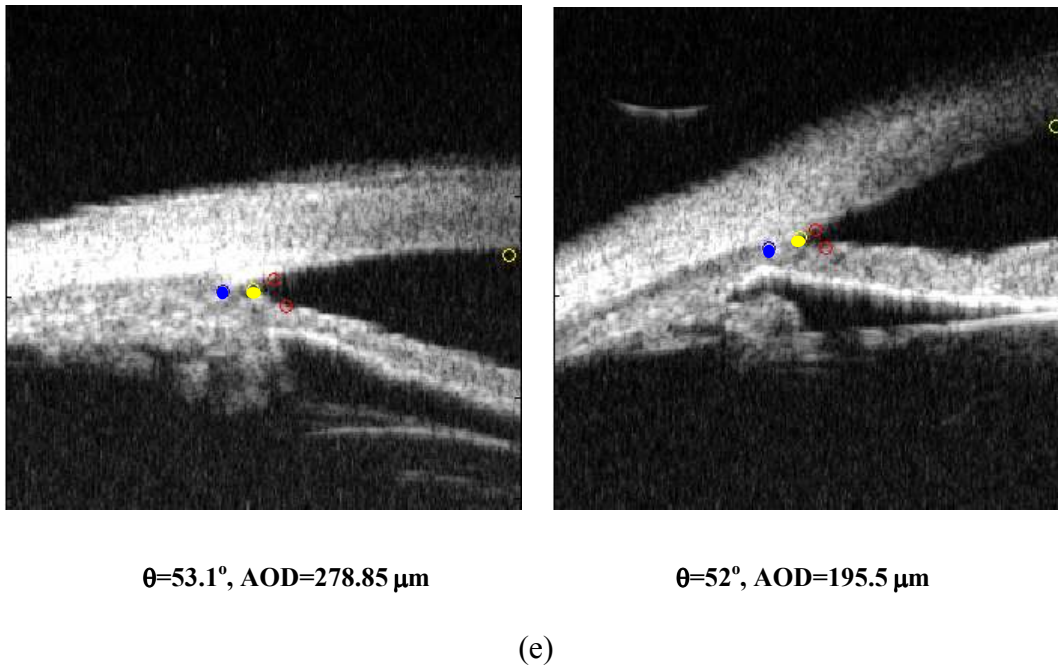


**Figure 50: Example of an outcome 2 (zero pixel offset error) where (a) Original image, (b) Segmented anterior chamber region, (c) Finely enhanced image, (d) Segmented sclera region. (e) Example of images with calculated parameters of interest**

### 7.3 An example of Outcome 3

This example illustrates a case where the segmentation of the sclera region succeeded but the clinical parameters computed differed from the technologist measurements by an offset error greater than  $97.5 \mu\text{m}$  in either direction (Figure 51 (f)). The main cause of the error is due to the minima locator that rejected the point on the contour map (Figure 51 (e)) corresponding to the real location of the scleral spur. This point was disqualified from the set of possible values since it is situated at the boundary of the signal and its derivative does not exist. The pixel offset error is  $135 \mu\text{m}$  and  $405 \mu\text{m}$  in the vertical and horizontal direction, respectively (Figure 51 (f)).

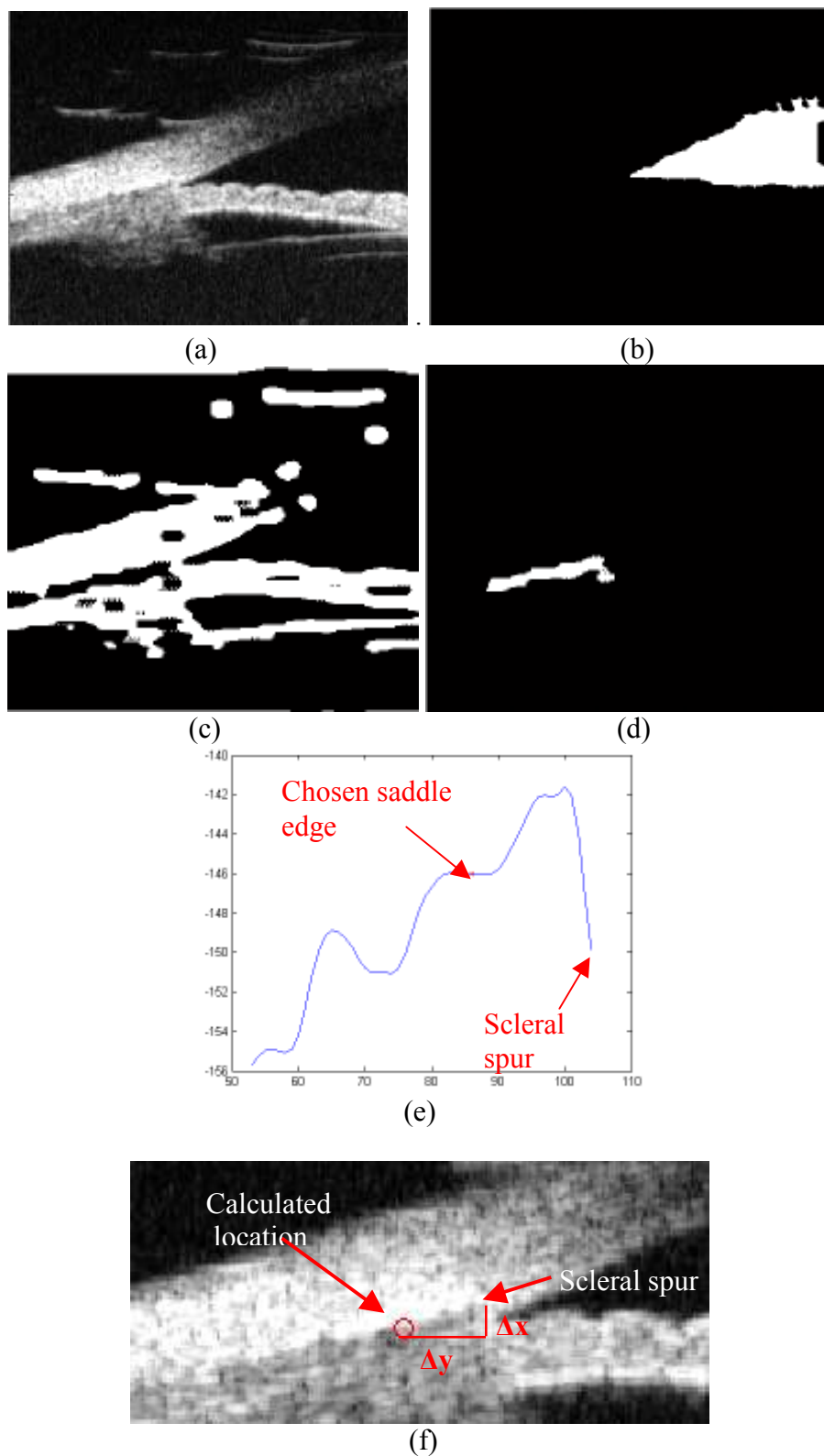


Figure 51: Example of an outcome 3 (pixel offset error  $>97.5\mu\text{m}$ ) where (a) Original image, (b) Segmented anterior chamber region, (c) Finely enhanced image, (d) Segmented sclera region, (e) Calculated scleral spur coordinates and real scleral spur location, (f) Pixel offset error ( $\Delta x=135\ \mu\text{m}$ ,  $\Delta y=405\ \mu\text{m}$ )

# Chapter 8

## Discussion

This thesis has developed an algorithm to automatically identify features in ultrasound images of the eye and compute the clinical parameters of interest to the technologist. Many algorithms have been proposed in order to enhance and detect features in ultrasound images (Mohammed *et al*, 2003, Pathak *et al*, 2000); however, none have specifically addressed feature detection in iris images. The algorithms chosen in this work were those found experimentally to give good results. In developing this work, several different approaches were tested in order to select the algorithm presented in Chapter 6. Based on the results obtained from testing the developed method on sample images, we believe that the accuracy of the algorithm could be further improved by adjusting the saddle and minima locator technique described in section 6.3.6. Applying the filtering operations of the multiscale algorithm in the frequency domain can further reduce the processing time of the algorithm. For each image, a 9x9 Gaussian low pass filter is used and applied for 8 iterations in the spatial domain.

Because of the large body of work on ultrasound image processing algorithms, we feel that it is valuable to briefly review and comment on the applicability of these algorithms to the problem considered in this thesis.

Recently, there has been active research on image denoising and speckle reduction in ultrasound and Synthetic Aperture Radar (SAR) images. Xie *et al* (2002) proposed a

spatially adaptive noise reduction algorithm that is constructed for image denoising using a combination of wavelet Bayesian methods and a Markov random field image regularization technique. Ulfarsson *et al* (2002) presented a speckle-reduction algorithm that is proposed in the Curvelet domain where a threshold is applied on the coefficients for the denoising process. In Saevarsson *et al* (2004) a fusion of the undecimated discrete wavelet transforms (UDWT) and a time invariant discrete curvelet transform (TIDCT) is used for speckle-reduction in SAR images. These methods perform well for image denoising but to achieve proper texture segmentation in ultrasound images, additional edge enhancement techniques should be applied.

Many other techniques exist for ultrasound image denoising. For example, Xie *et al* (2002), Ulfarsson *et al* (2002), Saevarsson *et al* (2004) are based on processing in wavelet domain where the selection of a wavelet mother basis depends on the application. These techniques focused uniquely on speckle reduction. Zong *et al*, (1998) proposed a speckle reduction and contrast enhancement in the wavelet domain. The noise reduction was obtained by soft thresholding the wavelet coefficients and feature enhancement was accomplished via nonlinear stretching followed by hard thresholding of wavelet coefficients within selected spatial-frequency levels. The technique showed good results for visual image improvement, but feature identification and segmentation were not explored. Also, wavelet coefficients thresholding leads to the appearance of parasitic oscillations in the vicinity of edges. Bezvesilniy *et al* (2003) proposed a wavelet-based image processing, edge detection and noise reduction technique. This method overcomes the oscillation problem by using a first derivative of the cubic B-spline as the analyzing

wavelet. This led to well-behaved edge representation in the wavelet domain where edges are sharp and well localized and do not have oscillations. This approach also allows edge classification and processing based on edge height. However, this approach may not be stable in the presence of ultrasound speckle noise. This is because texture analysis in ultrasound images is difficult, especially in an application such as this, due to the poor boundary delineation near the sclera tissue.

Other existing methods that combine denoising, enhancement and feature detection of ultrasound images include the use of Gabor filter texture segmentation (Mohamed *et al*, 2004, Xie *et al*, 2005) and diffusion filter and *sticks* (Pathak *et al*, 2000). Mohamed *et al* (2003) tuned and applied the spatial parameters of the Gabor filter to Trans-rectal ultrasound images of the prostate (TRUS) such that the filter output magnitude matches the desired texture. The outline of a cancerous region is then segmented by providing the algorithm some texture information. In order to capture all texture areas, large filter banks are required to analyze the image. Xie *et al* (2005) developed a method for kidney segmentation based on texture analysis by applying a bank of Gabor filters to process the ultrasound image, based on proper modeling of shape priors for segmentation. In this technique, the initial segmenting curves were positioned manually requiring the input of trained users for each image.

Another approach in ultrasound defines line segments called *sticks* (Pathak *et al*, 2000) in different angular orientations as templates that model false edges while reducing speckle. The technique allows contrast enhancement only at the edges, while noise is decreased. An anisotropic diffusion filter is used to further smooth the image and reduce noise to

allow for Canny edge detection. The method allows a technician to overlay the detected edges on the original image to assist manual delineation of the prostate. The methods reviewed can be generally used to process the ultrasound images. However, fully automated techniques were not developed to detect and extract the areas of interest, which was the main objective of this thesis.

## **8.1 Other areas of application**

The underlying technique developed in this thesis could also be used to enhance ultrasound images in other applications. To explore this possibility, the algorithm was tested on a prostate ultrasound image to enhance contrast and edges while reducing noise. This task is important since accurate detection of the prostate boundaries is required in many treatment procedures of the prostate disease (Pathak *et al*, 2000). Image enhancement and good edge delineation are crucial for automatic edge detection. In Pathak (2000), the *sticks* method is used to enhance contrast and to reduce speckle noise in the ultrasound prostate image. The result is then further smoothed using an anisotropic diffusion filter (Figure 52 (b)). For comparison, the same image (Figure 52 (a)) is enhanced using our multiscale algorithm for 5 iterations. The resultant image (Figure 53) shows good edge delineation around the prostate region as well as better contrast.

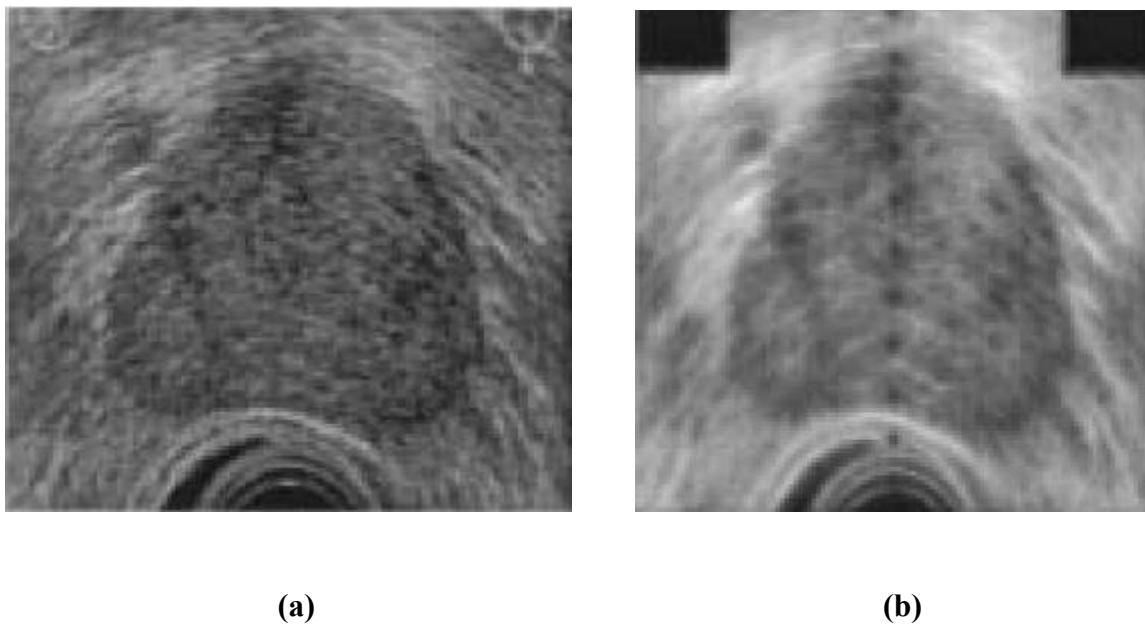


Figure 52: The result of applying the sticks algorithm of Pathak (2000) on an ultrasound prostate image. (a) Original image (b) Enhanced image using a 45 pixel long stick (*taken from Pathak (2000)*)

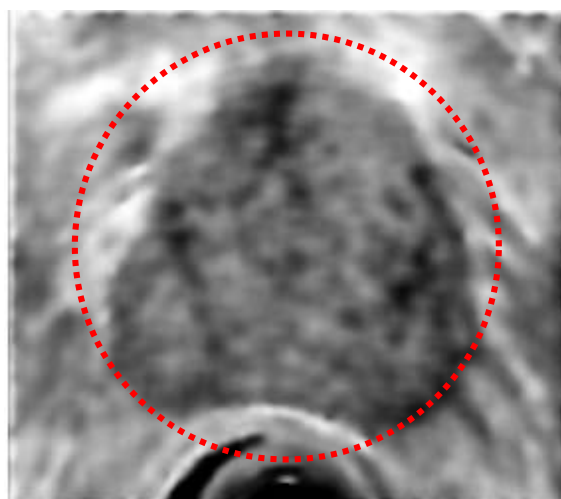
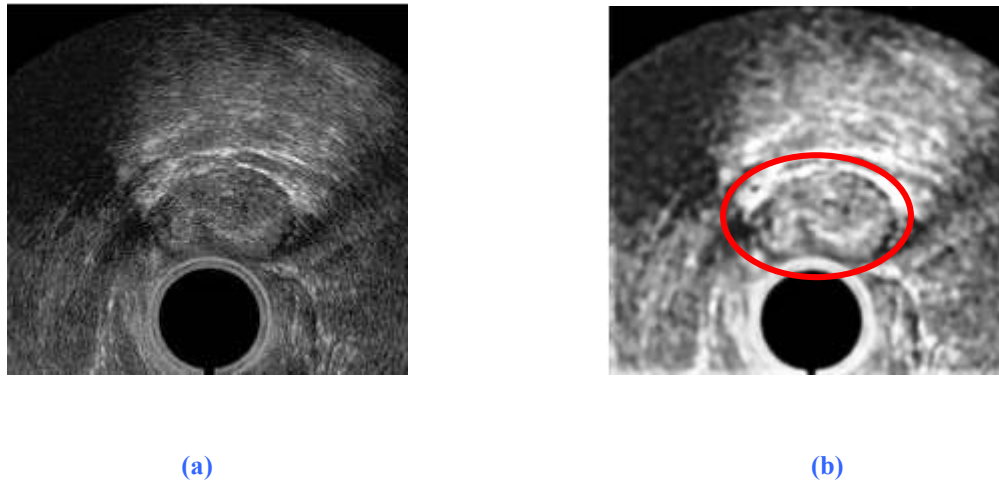


Figure 53: Enhanced prostate ultrasound image using our developed algorithm for 5 iterations. S-parameters are  $s_1=s_2=s_3=0.01$ ,  $s_4=5$ ,  $s_5=10$  and  $c=140$ . The region of interest is outlined.

Another example of image enhancement using the algorithm of this thesis is seen in Figure 54. The enhanced image (Figure 54 (b)) shows better edge delineation than the original image and a better contrast, which facilitates prostate segmentation.



**Figure 54:** Ultrasound images of the prostate (*taken from [www.rad.upenn.edu/~yzhan/ProstateSegmentation](http://www.rad.upenn.edu/~yzhan/ProstateSegmentation)*) (a) Original (b) Enhanced using multiscale algorithm for 5 iterations. S-parameters are  $s_1=s_2=0$ ,  $s_3=3$ ,  $s_4=5$ ,  $s_5=6$  and  $c=145$ .

## 8.2 Future work

In ultrasound imaging, speckle noise severely degrades the visual quality of the image. In order to achieve high accuracy when extracting features, speckle must be filtered without destroying any important characteristics in the image. In our developed algorithm, speckle noise was reduced using an a multi-scale algorithm with an adaptive wiener filter that applies a weighted average calculation using sub-region statistics to estimate statistical measures over a fixed 9x9 window. It is worthwhile to investigate a different speckle reduction technique that do not depend on the selection of the window size and that can be used on the ultrasound images of the eye before edge enhancement.

One easy way to reduce speckle is to average multiple uncorrelated images of the same object obtained from different spatial positions. However, this procedure is computationally costly and will increase the processing time of the algorithm.

A more efficient way is to use the geometric filter of Crimmins (1985) for speckle reduction. It seems to be a good replacement of the Wiener filter prior to fine enhancement since it does not require the selection of a fixed window size and it reduces speckle noise based on each pixel surrounding area. The non-linear geometric filter operates in four directions (horizontal, vertical, 2 diagonal) by sliding a window of varying size (3x3, 5x5, and 7x7) and calculating the minimum and maximum intensities for every direction. Then, the algorithm undergoes a series of pair wise operations in which it modifies the value of the center pixel by comparing, in turn, with each set of neighbors (N-S, E-W, NW-SE, NE, SW) in a search for intensity spikes. The geometric filter raises pixels that are darker than their surrounding neighbors and lower the ones that are brighter than their neighborhood to reduce the speckle index of the image (Loisou, 2003). Hence, pixel intensity adjustment is not biased by outliers that can be located in a specific area of the image since various window sizes are used. In general, this filter performs very well by repeated application on the image (3-4 iterations). However, for images with very poor resolution, more iterations can be applied until all pixels lying in the same local neighborhood have similar intensity values close to the initial spike value. If this technique shows improvement in speckle reduction and does not destroy edges in the original image, the enhancement process in our algorithm will require fewer iterations, resulting in a considerable reduction of the processing time.

Another future avenue of work would be to enhance the developed algorithm to compute other UBM parameters that are of interest to examine patient's eye after eye surgery or for a dose-response study using different drugs (Marchini, 2003). For example, the parameters in Figure 55 are normally computed to determine if laser iridotomy altered the anterior segment anatomy of patients with plateau iris configuration (Polikoff, 2005). Also, other parameters are studied to examine how iris thickness varies in response to drug injection as shown in Figure 56.

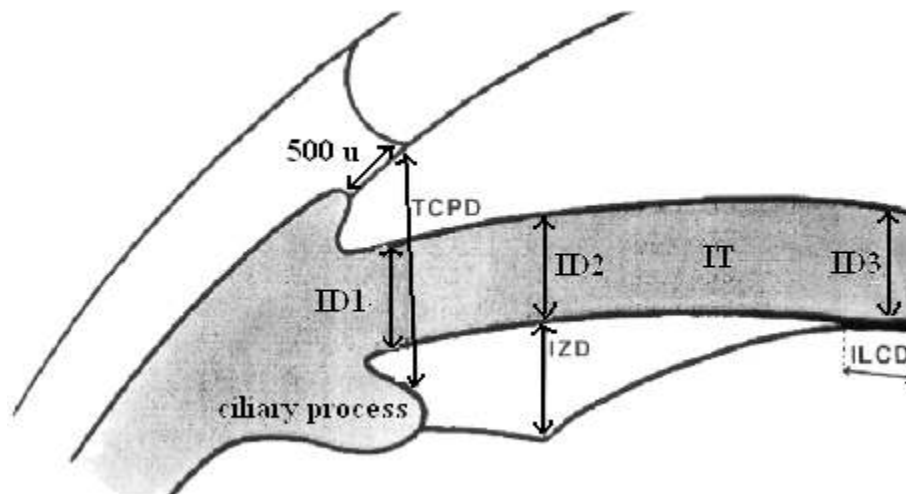


**Figure 55: Clinical UBM parameters. Trabecular-ciliary process distance (TCPD); Iris thickness (IT); Iris-ciliary process distance (ICPD); Iris-zonule distance (posterior chamber depth) (IZD); Iris-lens contact distance (ILCD) (taken from [www.iovs.org/cgi/](http://www.iovs.org/cgi/))**

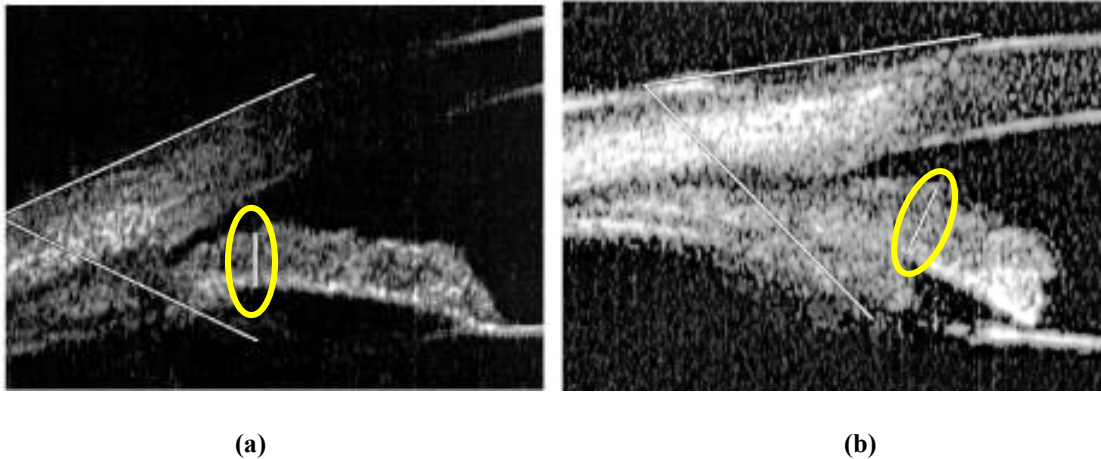


**Figure 56: Iris thickness before (a) and after (b) treatment with 2% ibopamine (taken from [www.iovs.org/cgi/](http://www.iovs.org/cgi/))**

The UBM parameters can be computed on the enhanced image using our algorithm such that the first measurement positions of the iris (ID1) is located on a line perpendicular to the iris connecting a point on the trabecular meshwork 500  $\mu\text{m}$  from the scleral spur to the ciliary process (TCPD). The second distance (ID2) is measured 2 mm from the scleral spur. The third (ID3) is measured at the thickest point near the iris margin. The TCPD distance is an important measurement and corresponds usually to  $1122 \pm 232 \mu\text{m}$  (Pavlin, 1995). This distance defines the port through which the iris must traverse and has implications as to the potential maximum angle opening. Other UBM parameters in different applications are described in more details by Pavlin (1995) and Marchini (2003). In order to compute these parameters using our algorithm, the ciliary process (Figure 55) must be located and then the texture information analyzed in that area before enhancement. This is feasible since the anterior chamber and scleral spur would already be detected, which help to locating other regions in the ultrasound image of the eye.

### 8.3 Conclusion

This thesis proposes an algorithm to automatically identify clinical features in ultrasound images of the eye. The algorithm computes the AOD 500 and the open-angle parameters used to measure the presence and severity of glaucoma. Overall, the algorithm predictions are very similar to the trained technologist's observation with a small ( $\pm 0.1$ mm) pixel offset error in both the horizontal and vertical directions. In the processed images, features were correctly identified in 97% of the cases. 3% of images presented inaccurate approximation of the clinical parameters, with 351  $\mu$ m error average. The difficulties encountered in measuring clinical parameters are associated with the speckle noise, poor contrast, poor resolution, and weak edge delineation present in the processed ultrasound images. These issues introduced inaccuracy in locating the scleral spur and variability in the measurement of the clinical parameters. The algorithm was designed with a goal of robustness through the use of two-stage (coarse and fine) level enhancement on the original image, and by validation of the proper segmentation of the sclera at each step. Overall, the benefit of this work is the ability of algorithm to reduce the processing time and improve processing consistency for each patient's ultrasound image, leading hopefully to an increase in efficiency and a reduction of cost.

## Bibliography

American Academy of Ophthalmology (2000) Primary angle closure, *American Academy of Ophthalmology*, San Francisco

Anderson M, Trahey G (2000) A seminar on k-space applied to medical ultrasound, *Department of Biomedical Engineering*, Duke University

Baum G (1956) The effect of ultrasonic radiation upon the eye and ocular adnexa, *Am J Ophthalmol* **42** 696-706

Begui Z E (1954) Acoustic properties of refractive media of the eye, *J Acoust Soc Am*, **26** 365-372

Bezvesilniy O, Vinogradov V, Vavriv D, Schunemann K (2003) Wavelet-based image processing: edge detection and noise reduction, *17th International Conference on Applied Electromagnetics and Communications*, 123 – 126

Bovik A L (2000) Handbook of Image & Video Processing, *Academic Press*, Texas

Coleman D J, Lizzi F L, Jack R L (1977) Ultrasonography of the Eye and Orbit, *Lea & Febiger* Philadelphia

Crimmins T (1985) The Geometric Filter for Speckle Reduction, *Applied Optics* **24** 10

Damji K F, Bains H S, Stefansson E (1998) Is pseudoexfoliation syndrome inherited? A review of genetic and nongenetic factors and a new observation, *Ophthalmic Genetics* **19** 175-185

Daneshvar H, Brownstein S, Mintsioulis G, Chialant D, Punja K, Damji K F (2000) Epithelial in growth following penetrating keratoplasty: A Clinical, Ultrasound Biomicroscopic and Histopathological Correlation, *Canadian Journal of Ophthalmology* **35** 222-224

Deepak B (2002) Ultrasound Biomicroscopy, *Journal of the Bombay Ophthalmologists Association* **12** 1-4

Deng G, Cahill L W (1994) Image Enhancement Using the Log-ratio Approach, *Signals Systems and Computers* **1** 198-202

Deng G, Cahill L W (1993) Multiscale image enhancement using the logarithmic image processing model, *Electronics Letters* **29** 803-804

Deng G, Cahill L W, Tobin G R (1995) The study of logarithmic image processing model and its application to image enhancement, *IEEE Transactions on Image Processing* **4** 506-512

Forster F K, Olerud J E, Pomajevich G R, Holmes A W, Sharar S R (1986) High-frequency ultrasonic imaging and backscatter attenuation techniques for determination of thermal injury to the skin, *IEEE Ultrasonics Symposium Proceedings* **2** 957-962

GE Healthcare Bio-sciences (2004) *Pulse-echo imaging*. Retrieved July 17,2005 from <http://www.amershamhealth.com/medcyclopaedia/medical>

Goss S A, Johnston R L, Dunn F (1978) Comprehensive compilation of empirical ultrasonic properties of mammalian tissues, *Journal of the Acoustical Society of America* **64** 423-457

Heath M (1999) *An introduction to ultrasound physics for general practitioners*. Retrieved July 12, 2005 from <http://www.sci.port.ac.uk/>

Hosgson J M, Graham S P, Savakus A D, Dame S G, Stephens D N, Brand B, Sheehan H, Eberle M J (1989) Clinical percutaneous imaging of coronary anatomy using an over-the-wire ultrasound catheter system, *Int J Card Imaging* **4** 186-193

Jansson F, Sundmark E (1961) Determination of the velocity of ultrasound in ocular tissues at different temperatures, *Acta Ophthalmol* **39** 899-911

Lim J S (1990) Two-dimensional Signal and Image processing, *Englewoods Cliffs Prentice-Hall*, New Jersey

Loizou C, Pattichis C S, Istepanian R, Pantziaris M, Kyriakou E, Tyllis T, Nicolaide A (2003) Ultrasound image quality evaluation, *Proc of the 4th Annual IEEE Conf on International Technology Applications in Biomedicine* 138-141

Mohamed S S, Abdel-galil T K, Salama M A, Fenster A, Downey D B, Rizkalla K, El-saadany E F, Karmel M (2003) Prostate Cancer Diagnosis Based on Gabor Filter Texture Segmentation on Ultrasound Image, *IEEE Canadian Conference on Electrical and Computer Engineering*, 1485-1488

Mundt G H, Hughes W F (1956) Ultrasonics in ocular diagnosis, *Am J Ophthalmol* **42** 488-498

Nicholas D (1977) An introduction to the theory of Acoustic Scattering by Biological Tissue, in *Recent Advances in Ultrasound in Biomedicine*, Forest Grove, OR

Nishijima K, Takahashi K, Yamakawa R (2000) Ultrasound Biomicroscopy of the Anterior Segment after Congenital Cataract Surgery, *American Journal of Ophthalmology* **130** 483-491

Ossoinig K C (1979) Standardized echography: Basic principles, clinical applications, and results, *Int Ophthalmol Clin* **19** 127-210

Pathak P D, Chalana V, Haynor D H, Kim Y (2000) Computer-aided edge guidance for prostate delineation, *IEEE Transaction on Medical Imaging* **19** 1211-1219

Loizou C, Christodoulou C, Pattichis C S, Istepanian R, Pantziaris M, Nicolaides A (2002) Speckle Reduction in Ultrasound Images of Atherosclerotic Carotid Plaque, *IEEE 14th International Conference on Digital Signal Processing* **2** 525-528

Marchini G, Babighian S, Tosi R, Perfetti S, Bonomi L (2003) Comparative Study of the effects of 2% Ibopamine, 10% Phenylephrine, and 1% Tropicamide on the Anterior Segment, *Investigative Ophthalmology and Visual Science* **44** 281-289

Nishijima K, Takahashi K, Yamakawa R (2000) Ultrasound biomicroscopy of the anterior segment after congenital cataract surgery, *American Journal of Ophthalmology* **4** 483-492

Pandian N G (1989) Intravascular and intracardiac ultrasound imaging: An old concept, now on the road to reality, *Circulation* **2** 1091-1094

Pathak S D, Chalana V, Haynor D R, Kim Y (2000) Edge-Guided Boundary Delineation in Prostate Ultrasound Images *IEEE Transactions on Medical Imaging* **19** 1211-1219

Pavlin C J, Foster F S (1995) Ultrasound Biomicroscopy of the eye, 1st ed, *Springer-Verlag*, New York

Pavlin C J, Harasiewicz K, Sherar MD, Foster FS (1991) Clinical Use of Ultrasound Biomicroscopy, *Ophthalmology* **98** 287-295

Polesel A, Ramponi G, Mathews V J (2000) Adaptive unsharp masking for contrast enhancement, *IEEE Transactions on Image Processing* **9** 505-510

Polikoff LA, Chanis RA, Toor A, Ramos-Esteban JC, Fahim MM, Gagliuso DJ, Serle JB (2005) The effect of laser iridotomy on the anterior segment anatomy of patients with plateau iris configuration, *Department of Ophthalmology* **14** 109-122

Rivara A, Sanna G (1962) Determination of the velocity of ultrasound in ocular tissues of human and swine, *Ann Ottalmol Clin Ocul* **88** 675-680

Saevarsson B B, Sveinsson J R, Benediktsson J A (2004) Combined Wavelet and Curvelet Denoising of SAR Images, *Proceedings of the International Geoscience and Remote Sensing Symposium (IGARSS)* **6** 4235 – 4238

Sherer MD, Starkoski B G, Taylor W B, Foster F S (1989) A 100 Mhz B-scan ultrasound backscatter microscope, *Ultrasound Imaging* **11** 95-105

Silverstein F E et al. (1989) Experimental evaluation of an endoscopic ultrasound probe : In vitro and in vivo canine studies, *Gastroenterology* 1052-1062

Thijssen M J, Mol M J, Timer M R (1983) Acoustic parameters of ocular tissues, *Ultrasound Med Biol* **11** 157-161

Ulfarsson M O, Sveinsson J R, Benediktsson J A (2002) Speckle reduction of SAR Images in the Curvelet Domain, *Proceedings of the International Geosciences and Remote Sensing (IGARSS)* **1** 315-317

Wiersema M J et al. (1989) Twenty-five MHz Gastrointestinal ultrasonography, *IEEE Ultrasonics Symposium Proceedings* 848-848

Woodcock J P (1979) Ultrasonics, *Medical Physics Handbooks*, Adam Hilger Ltd, Bristol

Xie J, Jiang Y, Tsui H (2005) Segmentation of kidney from ultrasound images based on texture and shape priors, *IEEE Transactions on Medical Imaging* **24** 45 – 57

Xie H, Pierce L E, Ulaby F T (2002) SAR Speckle Reduction Using Wavelet Denoising and Markov Random Field Modeling, *IEEE Transactions on Geosciences and remote sensing* **40** 2196-2212

Yano T, Fukukita H, Uneo S, Fukomoto A (1987) 40 MHz. ultrasound diagnostic system for: Dermatologic Examination, *IEEE Ultrasonics Symposium Proceedings* **2** 875-878

Ye S G, Harasiewicz K A, Pavlin C J (1995) Ultrasound characterization of ocular tissue in the frequency range from 50 MHz to 100MHz, *IEEE Transactions on Ultrasonics Ferroelectrics and Frequency Control* **42** 8-14

Yock P G, Linker D T, Angelsen B A (1989) Two dimensional intravascular ultrasound: Technical development and initial clinical experience, *J Am Soc Echo* **2** 296-304

Zong X, Laine A F, Geiser E A (1998) Speckle reduction and contrast enhancement of echocardiograms via multiscale nonlinear processing, *IEEE Transactions on Medical Imaging* **17** 532 – 540

## Appendix 1: Scleral Spur detection Matlab Code

Appendix 1 lists the Matlab code used for detection of the scleral spur. The main function is *scleral\_spur\_detection.m* which implements the method described in chapter 7.

```
% Read image of size 5mm x5mm
im=double(imread('eye.pcx'));

% Resolution taken from ultrasound machine. Conversion from pixel to mm.
x_pixel_to_mm = 5.0 / imSize_x;
y_pixel_to_mm = 5.0 / imSize_y;
[x_grid, y_grid] = meshgrid(1:imSize_x, 1:imSize_y);

% Call function "region_triangle" to segment the anterior chamber
[good_region, stats, bf_labeled_im, y_min, x_min_triangle, x_max_triangle, y_min_triangle,
y_max_triangle, reg_before_bwfill, x_max_close_to_y_min]=region_triangle(im);

% Extract the trace of the scleral on the image generated after isolating the central region of the eye
row_edge_loc = [];
col_edge_loc = [];
col_index = 1;
for col_dir = 1:imSize_x,

located_one = find(tm_region_1(:,col_dir) == 1);

% Only store the trace that has been detected by the edge filter.
% Treat all other parts of the trace as discontinuities. That is,
% any column vectors not containing a value will not be considered
% as part of the trace of the ciliary body or iris. "Isempty" will
% be used to validate this. Returns a "1" if it is an empty column
% vector.

if isempty(located_one) == 0

    located_one = located_one(1,1);
    row_edge_loc(col_index,1) = located_one;
    col_edge_loc(col_index,1) = col_dir;
    col_index = col_index + 1;
end

end

% Any sharp changes in slope appear to be in the region of the trabecular
% meshwork. The round hump in the image. Calculate the derivative to examine
% this change in slope and locate only those changes that define the
% trabecular meshwork and scleral.
th_dev_level = 16.5;
```

```

tm_col_loc_derv = [];
tissue_not_found = isempty(tm_col_loc_derv);
while (tissue_not_found)

    delta_col_edge_loc = diff(col_edge_loc);
    tm_locations = find(abs(delta_col_edge_loc) > th_dev_level);
    tm_col_loc_derv = col_edge_loc(tm_locations,1);
    tm_row_loc_derv = row_edge_loc(tm_locations,1);

    tissue_not_found = isempty(tm_col_loc_derv);
    if (tissue_not_found == 1)
        th_dev_level = th_dev_level / sqrt(2);
    end

end

tm_col_loc = mean(tm_col_loc_derv);
tm_row_loc = mean(tm_row_loc_derv);
tm_vector = [tm_row_loc tm_col_loc];

% Sclera segmentation using function "region_scleral.m"
[good_region,stats,bf_labeled_im]=region_scleral(im,y_min,      x_min_triangle,      x_max_triangle,
reg_before_bwfill,x_max_close_to_y_min);

idx2 = find([stats.Area]==stats(good_region).Area);
tm_region_2 = ismember(bf_labeled_im,idx2);

% Extract the trace of the scleral on the image generated after isolating the central region of the eye
row_edge_loc = [];
col_edge_loc = [];
col_index = 1;
for col_dir = 1:imSize_x,
    located_one = find(tm_region_2(:,col_dir) == 1);

    % Only store the trace that have been detected by the edge filter.
    % Treat all other parts of the trace as discontinuities. That is,
    % any column vectors not containing a value will not be considered
    % as part of the trace of the ciliary body or iris. Isempty will
    % be used to validate this. Returns a "1" if it is an empty column vector.

    if isempty(located_one) == 0

        located_one = located_one(1,1);

        row_edge_loc(col_index,1) = located_one;
        col_edge_loc(col_index,1) = col_dir;
        col_index = col_index + 1;
        diff_Size = col_index - 1;
    end

end

% Remove the edge samples as this would be a result of the above algorithm
% abruptly cutting the scleral. Also only look at 1/2 the length of the
% scleral on the right-hand side as this is where the spur is most likely
% to be.

```

```

reduced_col_edge_loc=col_edge_loc;
reduced_row_edge_loc=row_edge_loc;

%%To invert the graph
reduced_row_edge_loc=-1.*reduced_row_edge_loc;

% Perform a window smoothing on the edge samples to remove any small
% deviations that may appear as false detections within the gradient.

index=0;
order=1;
av_curve=0;

% Test filtering using 4th order butterworth
wn=0.45;

[B,A] = butter(4,wn);
fitted_row_edge_loc = filtfilt(B,A,reduced_row_edge_loc);
idx2 = find([stats.Area]==stats(good_region).Area);
tm_region_2 = ismember(bf_labeled_im,idx2);
[region_x,region_y]=find(tm_region_2>0);
min_y=min(region_y(:));
max_y=max(region_y(:));

offset=0;

if max_y>(y_min)
    offset=abs((y_min-10)-max_y);
end
mid_loc = floor((diff_Size) / 2);

stop=1;
xtra_pixel=4;

% In case there is not enough sample points
if (length(row_edge_loc) <120) | (offset >45)
    mid_loc = floor((diff_Size) / 4);
end

if (mid_loc > ((diff_Size-offset)-xtra_pixel )) | (max_y >230)
    mid_loc = floor((diff_Size) / 10);
end
reduced_col_edge_loc_temp = reduced_col_edge_loc((mid_loc:(diff_Size-offset)-xtra_pixel),1);
reduced_row_edge_loc_temp = reduced_row_edge_loc((mid_loc:(diff_Size-offset)-xtra_pixel),1);
fitted_row_edge_loc_temp = fitted_row_edge_loc((mid_loc:(diff_Size-offset)-xtra_pixel),1);
reduced_col_edge_loc=reduced_col_edge_loc_temp;
reduced_row_edge_loc=reduced_row_edge_loc_temp;
fitted_row_edge_loc=fitted_row_edge_loc_temp;
figure;
plot(reduced_col_edge_loc, reduced_row_edge_loc-mean(reduced_row_edge_loc), 'or',
reduced_col_edge_loc, fitted_row_edge_loc-mean(fitted_row_edge_loc), '*b');

% Find Descendant edges (all the points along that edge) and local minimas of the fitted data
y=fitted_row_edge_loc;
y_grad=gradient(y);

```

```

[rr,neg_edge]=minimas(y);

if length (rr)==1

    scleral_point=rr;
end

if length(rr)>1

[array,min_loc]=scleral_location(rr,neg_edge,y);
[s,d]=size(array);

for k=1:s,
    if sum(array(k,:) >0)

        [tx,ty]=find(array(k,.)~=0);
        min_val=min(array(k,ty));
        max_val=max(array(k,ty));
        slope_amp(k)=abs(y(min_val))- abs(y( max_val+1 ));
    end
end

[x_max_slope,y_max_slope]=find(abs(slope_amp)==max(abs(slope_amp)));
scleral_point=min_loc(y_max_slope);

% threshold on slope amplitude

if max(abs(slope_amp))<3 | (length(neg_edge)<6)
    rr=[];
    scleral_point=[];
    neg_edge=[];
end

% Saddle edge detection
if length(scleral_point)>1
    scleral_point=min_loc(max(y_max_slope));
end

if length(rr) <1
    disp('Saddle Point')

    [rr]=saddle(fitted_row_edge_loc);

    len=length(rr);
    stop=1;
    counter=1;
    track=[];
    i=1;

    while i<(length(rr))

        if abs((rr(i)-rr(i+1)))==1
            store_rr(counter,i)=rr(i);

        else

```

```

        store_rr(counter,i)=rr(i);
        counter=counter+1;
    end
    i=i+1;
end

if abs((rr(length(rr))-rr((length(rr)-1))))==1
    store_rr(counter,i)=rr(i);
else
    store_rr(counter,i)=rr(length(rr));
end

for k=1:counter
    length_array(k)=length(find(store_rr(k,:)>0));
end

stop=1;
num_points=4;
max_array=max(length_array);
max_len=[];

while stop==1
    max_len=find(length_array>num_points);

    if length(max_len)>0

        max_point_row=max_len(length(max_len));
        stop=0;
    else
        num_points=num_points-1;
        stop=1;
    end
end
coor_x=find(store_rr(max_point_row,:)>0);
temp_min=store_rr(max_point_row,min(coor_x));
temp_max=store_rr(max_point_row,max(coor_x));

scleral_point=floor(((temp_max)+(temp_min))/2);

if (isempty(scleral_point))(length(rr)==1)
    scleral_point=rr;
end
end
end

rr=round(rr);
neg_edge=round(neg_edge);
final_scleral_point=scleral_point+min(reduced_col_edge_loc)-1;

% Extract scleral tissue information
x_scleral=abs(reduced_row_edge_loc(scleral_point));
y_scleral=final_scleral_point;

% Find the 3 coordinates on the triangle region using function "coordinate.m"

```

```
[y_new_corner, x_new_corner, x_min_triangle, x_max_triangle, y_min_triangle,y_max_triangle,
x_middle_point, y_middle_point ] = coordinate(im, x_min_triangle, x_max_triangle,y_min_triangle,
y_max_triangle, x_max_close_to_y_min, y_min, tm_region_1, x_scleral, y_scleral);
```

## Appendix 2: Anterior Chamber region segmentation Matlab Code

Appendix 2 lists the Matlab code used for the segmentation of the anterior chamber in the ultrasound image of the eye. The main function is *region\_triangle.m*, which implements the method described in Chapter 7.

```
function [out1,out2,out3,out4,out5,out6,out7,out8,out9, out10]=region_triangle(im)
```

```
colour_grid_size = 256;
good_region=[];
```

```
imSize = size(im);
imSize_x = imSize(1,2);
imSize_y = imSize(1,1);
```

```
% Make the dimensions for the image square
```

```
if (imSize_x < imSize_y)
    imSize_y = imSize_x;
    im = im(1:imSize_x, 1:imSize_y);
else
    imSize_x = imSize_y;
    im = im(1:imSize_x, 1:imSize_y);
end
```

```
im = double(im);
```

```
% Resolution taken from ultrasound machine. Conversion from pixel to mm.
```

```
x_pixel_to_mm = 5.0 / imSize_x;
y_pixel_to_mm = 5.0 / imSize_y;
[x_grid, y_grid] = meshgrid(1:imSize_x, 1:imSize_y);
```

```
%First Image (triangle enhancement)
```

```
im_original=im;
```

```
%Thresholding
```

```
for i=1:256,
    for j=1:256,
        if im(i,j)<50
            im(i,j)=0.1;
        end
        if im(i,j)>50
```

```

        im(i,j)=255;
    end
end

im1=im;
im1=imdilate(im1,strel('disk',1));
im=im1;

% Adaptive wiener filtering
[J,noise] = wiener2(im,[15 15]);

% Multiscale enhancement using log-ratio approach
[filt_im_low_10, all_images]=multiresolution_8(J, 0,0,0,100,100,50,80,200, 200);
[filt_im_low_3, all_images]=multiresolution_4(J ,0,100,100,200, 235);

% Threshold the filtered ("blurred") image
filtered_image = filt_im_low_3;
filt_im_size = size(filtered_image);
filt_im_size = filt_im_size(1,2);

thresh_ratio = 0.6; % Arbitrary threshold value --> seems to be effective
thresh_level = (max(filtered_image) - min(filtered_image) ) * thresh_ratio + min(filtered_image);
filt_im_binary_3 = [];
for index = 1:filt_im_size,
    filt_im_thresh = filtered_image(:,index) > thresh_level(1,index);
    filt_im_binary_3 = [filt_im_binary_3 filt_im_thresh];
end

% Threshold the filtered ("blurred")image
filtered_image = filt_im_low_10;
filt_im_size = size(filtered_image);
filt_im_size = filt_im_size(1,2);

thresh_ratio = 0.5; % Arbitrary threshold value --> seems to be effective
thresh_level = (max(filtered_image) - min(filtered_image) ) * thresh_ratio + min(filtered_image);
filt_im_binary_10 = [];
for index = 1:filt_im_size,

    filt_im_thresh = filtered_image(:,index) > thresh_level(1,index);
    filt_im_binary_10 = [filt_im_binary_10 filt_im_thresh];

end

% Remove little connections and artifacts in the image
temp_im_bin = filt_im_binary_10;
counter=1;

% First Pass (3 iterations, fine removal)
while counter<10

for z1=3:252,
    for z2=3:252,
        if temp_im_bin(z1,z2-2)==1 & temp_im_bin(z1,z2+2)==1
            temp_im_bin(z1,z2)=1;

```

```

    end
end
end

counter=counter+1;
end

%%Second pass (coarse removal)
counter=1;

while counter<10
for z1=6:250,
    for z2=6:250,
        if (temp_im_bin(z1,z2-5)==1 & temp_im_bin(z1,z2+5)==1) | (temp_im_bin(z1-1,z2)==1 &
temp_im_bin(z1+1,z2)==1)
            temp_im_bin(z1,z2)=1;
        end
    end
end
end

counter=counter+1;
end

%Third Pass
counter=1;

while counter<10
for z1=11:245,
    for z2=11:245,
        if (temp_im_bin(z1,z2-10)==1 & temp_im_bin(z1,z2+10)==1)
            temp_im_bin(z1,z2)=1;
        end
    end
end
end

counter=counter+1;
end
filt_im_binary_10=temp_im_bin;

% Dilation
filt_im_binary_10=imdilate(filt_im_binary_10,strel('disk',1));

% Hole filling
filt_im_fill_holes_3 = imcomplement(imfill(imcomplement(filt_im_binary_3),'holes'));
filt_im_fill_holes_10 = imcomplement(imfill(imcomplement(filt_im_binary_10),'holes'));

filt_im_fill_holes=reg_before_bwfill;

% backward filling
% Detect a region along the y direction to where there is a black region in order to use the "bwfill"
%operator.
% Step 2: Locate the Ciliary body behind and Edge Detect to trace the iris-ciliary region.
fill_x_location = 25;          % Arbitrarily choice
fill_y_location = 100;

stop=1;

```

```

while stop==1
while (filt_im_fill_holes(fill_x_location, fill_y_location) == 1)
    fill_x_location = fill_x_location + 2;
end

if filt_im_fill_holes(fill_x_location+4,fill_y_location+4)==0
bf_im_upper = bwfill(filt_im_fill_holes, fill_y_location, fill_x_location, 4);
stop=0;
else
    stop=1;
    fill_x_location=fill_x_location+4;
    fill_y_location=fill_y_location+4;

end
end

fill_x_location = imSize_y - 1;          % Arbitrarily choice
fill_y_location = 200;

% Detect a region along the y direction to where there is a black region in
% order to use the bwfill operator.

stop=1;
while stop==1

while (bf_im_upper(fill_x_location, fill_y_location) == 1)
    fill_x_location = fill_x_location - 2;
end

if filt_im_fill_holes(fill_x_location-4,fill_y_location-4)==0
stop=0;
else

    stop=1;
    fill_x_location=fill_x_location-4;
    fill_y_location=fill_y_location-4;
end
end

bf_im_total = bwfill(bf_im_upper, fill_y_location, fill_x_location, 4);

% Template Correlation for Triangular shape only
trian1=imread('just_trian_1.png');
trian1=double(trian1(:,1));
trian1=double(trian1>0);

trian2=imread('just_trian_2.png');
trian2=double(trian2(:,1));
trian2=double(trian2>0);

trian3=imread('just_trian_3.png');
trian3=double(trian3(:,2));
trian3=double(trian3>0);

```

```

trian4=imread('just_trian_4.png');
trian4=double(trian4(:,2));
trian4=double(trian4>0);

trian5=imread('just_trian_5.png');
trian5=double(trian5(:,2));
trian5=double(trian5>0);

% Correlation
filt_im_low_10=(bf_im_total);

filt_im_low_10=imdilate(filt_im_low_10,strel('disk',1));

%%Dilate Bottom of image to remove zone

fill_x_location=1;
fill_y_location=90;

for i=100:251
    if (filt_im_low_10(i,fill_y_location)==0) &(filt_im_low_10(i+4,fill_y_location)==0)...
        &(filt_im_low_10(i-4,fill_y_location)==0)& (filt_im_low_10(i,fill_y_location+4)==0)...
        &(filt_im_low_10(i,fill_y_location-4)==0)
        fill_x_location=i;
        break;
    end
end

filt_im_low_10 = bwfill(filt_im_low_10, fill_y_location, fill_x_location, 4);

con1=xcorr2(imcomplement(filt_im_low_10),imcomplement(trian1));
con2=xcorr2(imcomplement(filt_im_low_10),imcomplement(trian2));
con3=xcorr2(imcomplement(filt_im_low_10),imcomplement(trian3));
con4=xcorr2(imcomplement(filt_im_low_10),imcomplement(trian4));
con5=xcorr2(imcomplement(filt_im_low_10),imcomplement(trian5));

[x1,y1]=find(con1==max(max(con1)) );
[x2,y2]=find(con2==max(max(con2)) );
[x3,y3]=find(con3==max(max(con3)) );
[x4,y4]=find(con4==max(max(con4)) );
[x5,y5]=find(con5==max(max(con5)) );

x1=x1-20;y1=y1-10;x2=x2-20;y2=y2-10;x3=x3-20;y3=y3-10;x4=x4-20;y4=y4-10;x5=x5-20;y5=y5-10;

%%Averaging indices
[xx1,yy1]=find(y1>120& x1<200);
y1=y1(xx1);
x1=x1(xx1);

[xx2,yy2]=find(y2>120& x2<200);
y2=y2(xx2);
x2=x2(xx2);

[xx3,yy3]=find(y3>120& x3<200);
y3=y3(xx3);
x3=x3(xx3);

```

```

[xx4,yy4]=find(y4>120& x4<200);
y4=y4(xx4);
x4=x4(xx4);

[xx5,yy5]=find(y5>120& x5<200);
y5=y5(xx5);
x5=x5(xx5);

len_y=length(y1)+length(y2)+length(y3)+length(y4)+length(y5);
len_x=length(x1)+length(x2)+length(x3)+length(x4)+length(x5);

avg_y=(sum(y1)+sum(y2)+sum(y3)+sum(y4)+sum(y5))./len_y;
avg_x=(sum(x1)+sum(x2)+sum(x3)+sum(x4)+sum(x5))./len_x;

if avg_y<100 | avg_x>200 | avg_x<50
    return;
end

%%Spatial shift on y-axis to readjust the correlation point for proper
%%chamber detection
if avg_y<230
    avg_y=avg_y+10;
end

%%Region Classification using "bwlabel" and Segmentation

[bf_labeled_im,num_of_regions] = bwlabel(imcomplement(bf_im_total),8);
color_labeled_im = label2rgb(bf_labeled_im);

stats = regionprops(bf_labeled_im,'All');
allArea = [stats.Area];
allMajor = [stats.MajorAxisLength];
allMinor = [stats.MinorAxisLength];
allCentroid = [stats.Centroid];

% Assign Centroid Pixel Values
n=0;

for z=1:2:length(allCentroid),
    n=n+1;
    all_Centroid_y(n)=allCentroid(z);
    all_Centroid_x(n)=allCentroid(z+1);
end

max_length_major=max(allMajor);
max_length_minor=max(allMinor);

sorted_Area = sort(allArea);
sorted_Major = sort(allMajor);
sorted_Minor = sort(allMinor);

% Region segmentation
n=1;

for z=1:num_of_regions,

```

```

if (abs(all_Centroid_y(z)-avg_y)<50) &(abs(all_Centroid_x(z)-avg_x)<50) & (allArea(z) >200) ...
    & (allMinor(z)>10) & (allMajor(z)>25)

    good_regions_vec(n)=z;
    n=n+1;
end
end

temp=all_Centroid_x(good_regions_vec(1));
good_region=good_regions_vec(1);

if length(good_regions_vec)>1
    for z=1:length(good_regions_vec),

        if all_Centroid_x(good_regions_vec(z))<temp
            temp=all_Centroid_x(good_regions_vec(z));
            good_region=good_regions_vec(z);
        end
    end

else

good_region=good_regions_vec;
end

% Select the point most to the left of the triangular region
idx1 = find([stats.Area]==stats(good_region).Area);
tm_region_1 = ismember(bf_labeled_im,idx1);

[x_good,y_good]=find(tm_region_1>0);

[x_close_to_y_min,y]=find(tm_region_1(:,min(y_good))>0);

[x1,y1]= find(x_good== min(x_good));
[x2,y2]= find(x_good== max(x_good));

%Output computed parameters on the anterior chamber
out1 =good_region;
out2=stats;
out3=bf_labeled_im;
out4=min(y_good); %Most to the left
out5= x_good(x1(length(x1)));
out6=x_good(x2(length(x2)));
out7=y_good(x1(length(x1)));
out8=y_good(x2(length(x2)));
out9=reg_before_bwfill;
out10=max(x_close_to_y_min);

```